Wageningen University and Research

MSc thesis

Revisiting Raw Data Processing of Combined Optical-Microwave Scintillometers

Author
R (Robin) Stoffer BSc

Supervisor
Dr.ir. OK (Oscar) Hartogensis

August 2, 2018

Abstract

For many meteorological and hydrological applications large-scale surface observations of the sensible (H) and latent (LE) heat flux are required in heterogeneous areas. Promising devices to obtain those fluxes are combined Optical-Microwave Scintillometers (OMS), which can indirectly measure both H and LE along linear paths of several kilometers. In this study we revisited the required processing of raw data in order to further improve the accuracy of the calculated fluxes. To this end we used EC and OMS data from the meteorology observatory in Lindenberg (Eastern Germany) and surrounding area, which is known from the LITFASS field experiments (Beyrich et al., 2006, 2012, e.g.). Hereby, we focused on three specific issues:

1. Unwanted contributions to the raw scintillation signal, which are not related to H and LE. We developed a new systematic way to choose a suitable high-pass filter (HPF) and low-pass filter (LPF), together with a filter that removes erratic spikes. By comparing the resultant structure parameters of the refractive index, $C^2_{n,\lambda}$, from different filter combinations to the ones derived from experimental field data, we found that implementing a HPF is most important. However, implementing a LPF did not show a clear improvement. This is likely caused by the large variability present in the comparison of the OMS and field data.

2. The behaviour of the structure parameter of the refractive index, $C^2_{n,\lambda}$, as a function of Bowen ratio β. According to literature $C^2_{n,mw}$ shows a theoretical minimum around $\beta \approx 2-3$ (Leijnse et al., 2007; Ward et al., 2013), which could reduce the sensitivity of the OMS. To investigate this feature in a more detailed and systematic way, we first derived an analytical formula that explicitly describes $C^2_{n,\lambda}$ (scaled with the structure parameter of temperature, C^2_T) as a function of β and the correlation coefficient between temperature and humidity, r_{Tq}. This formula did not only allow us to investigate the minimum found in literature, but also enabled us to examine the behaviour of $C^2_{n,\lambda}$ as a function of β for negative r_{Tq} and optical wavelengths. Most notably, we discovered a second theoretical minimum for $C^2_{n,opt}$ around negative β close to 0. Subsequently, we explored the occurrence of this theoretical minimum and the one found in literature also experimentally by comparing the theoretical relationships to $C^2_{n,\lambda}$-values derived from EC-data. It appeared that both theoretical minima were indeed present in the experimental $C^2_{n,\lambda}$-values, but will likely not pose a problem for the sensitivity of the OMS.

3. The robustness of the bichromatic method described by Lüdi et al. (2005). The bichromatic method is sensitive to inaccuracies: sometimes r_{Tq} shows chaotic behaviour and unrealistic values (Ward et al., 2015a). Therefore, we developed a new hybrid method that combines the bichromatic method with the two-wavelength method described by Hill (1997). It appeared that only changes in the sign of r_{Tq} between the bichromatic and hybrid method influenced the calculated surface fluxes substantially. The hybrid method was as a consequence mainly beneficial when the bichromatic method showed erratic sign-changes of r_{Tq}.

Contents

1 Introduction

Many hydrological and meteorological applications rely on models that take into account the surface sensible (H) and latent heat flux (LE) on a large-scale. Both H and LE are important components of the energy balance, while evapotranspiration (E) (and hence the energy equivalent LE) is important for the water balance. Representative large-scale observations of H and LE are thus crucial to validate and improve predictions from hydrological and meteorological models, especially when they are applied to heterogeneous areas. Typical examples include urban surface energy balance models (Masson, 2006, e.g.), water resource assessment models (Xu and Singh, 2004, e.g.), and crop-growth models (Mo et al., 2005, e.g.). An important technique currently often applied to measure H and LE is Eddy-Covariance (EC), where at a single station fluctuations of wind speed, temperature, and water vapour are sampled with a very high frequency (∼10-20 Hz). The sampled fluctuations are associated with turbulent motions called eddies, which are the main transport mechanism in the atmospheric boundary layer (ABL)[1].

The disadvantage of the EC-technique is that the measured fluxes do not necessarily represent the fluxes on larger scales as they are only measured at a single location. In other words, the footprint[2] of an EC-station is relatively small (∼0.001-1 km^2) and covers often only a small fraction of the study area for which large-scale fluxes are desired. This is not a problem in homogeneous areas like flat grassland, where the fluxes are expected to be quite constant in space. However, for many meteorological and hydrological applications large-scale fluxes are needed in heterogeneous areas like cities, where the spatial variability of the fluxes is large. As a result, the size and location of the footprint become critical to the fluxes that are measured. To overcome this issue of EC-measurements in heterogeneous rural areas, some studies used a network of EC-stations installed such that their footprints covered (partly) the spatial variability (Meijninger et al., 2002; Beyrich et al., 2006). These networks are impractical and expensive to use for continuous measurements during long time-periods though, especially for extremely heterogeneous areas like cities.

[1] According to Stull (1988), the ABL can be defined as "that part of the troposphere that is directly influenced by the presence of the earth's surface, and responds to surface forcings with a time-scale of about an hour or less".

[2] The footprint is defined as the area that contributes most to the measured fluxes; the exact size and location depend on the measurement height, wind direction, stability of the atmosphere, and the roughness of the surface (Leclerc and Thurtell, 1990, e.g.).

Another way to measure H and LE is to make use of satellite data (Bastiaanssen et al., 1998, e.g.). The advantage is that the measured H and LE are representative for larger scales than the ones measured by an EC-station. The disadvantage however is that the surface fluxes cannot be determined continuously. Also, the algorithms used to derive the surface fluxes from the data need to be validated.

A third technique to measure H and LE technique is scintillometry, which allows to measure H and LE along linear paths varying from 50 meters to several kilometers. Therefore, they have the potential to complement the small-scale EC-measurements and large-scale satellite data. In several studies scintillometers have been quite successfully applied to heterogeneous areas (Meijninger et al., 2006; Ward et al., 2015b, e.g.).

The measurement devices used in scintillometry, called simply scintillometers, send a light beam of a certain wavelength through the atmosphere that is refracted due to differences in temperature and humidity content. These differences are in turn linked to the surface fluxes H and LE (for a more detailed explanation see Section 2.1). Hence, the measurements of the scintillometers are only indirectly affected by H and LE.

This indirect effect of H and LE on the measurements depends on the wavelength of the light beam. In general, the scintillometers operate in either the optical/near-infrared or microwave range. The optical scintillometers are mainly sensitive for H, while microwave scintillometers are sensitive to both H and LE. Hence, to determine both H and LE the optical and microwave scintillometers are combined in several studies (Green et al., 2000; Meijninger et al., 2002; Ward et al., 2015b, e.g.). Another approach is to use only a single optical or microwave scintillometer in combination with an energy balance method, relying on auxiliary measurements of the total available energy (Meijninger et al., 2002; Leijnse et al., 2007, e.g.).

Since scintillometers measure H and LE indirectly, a theoretical framework is required with multiple processing steps to determine from the raw data eventually H and LE. Hereby, some issues still remain that can negatively affect the quality of the resultant fluxes. This is especially the case for combined optical-microwave scintillometers, as a more extensive framework is required and the development started more recently than for single optical scintillometers.

The aim of this research is therefore to improve the processing of raw data from optical-microwave scintillometers to fluxes. To serve this aim, we will investigate three different issues. These are introduced with their corresponding research questions in Section 3.

In Section 2 we will explain the measurement principle of a scintillometer together with the steps involved in the processing of the raw data. Subsequently, we will discuss in Section 5 the applied methodology and the results for each research question separately. Finally, in Sections 6 and 7 we give the main conclusions and recommendations respectively.

2 Theory

2.1 Measurement principle of combined optical-microwave scintillomters

The measurement principle of combined optical-microwave scintillometers (OMS) is sketched in Figure 1: a transmitter sends a light beam of a certain wavelength (either in the optical or microwave range) through the atmosphere towards a receiver. Along this transect, the light beam crosses multiple turbulent eddies with differences in both temperature and humidity related to the surface fluxes H and LE. Consequently, the refractive index (n) differs between the different eddies as the refractive index depends on temperature and humidity. This dependency changes with different wavelengths of the light beam: the refractive index is mainly sensitive to temperature differences in the optical range, while it is sensitive to both temperature and humidity differences in the microwave range.

The resulting wavelength-dependent differences in refractive index cause the light beam to be refracted while it travels from the transmitter towards the receiver. As a consequence, at the receiver the light beam exhibits intensity fluctuations that scale with the size of H and, in case of microwave wavelengths, LE. This implies that H and LE can be indirectly determined relying on the measured intensity fluctuations of both an optical and microwave scintillometer. Hereby multiple processing steps are needed (Figure 1), which will be briefly described in Section 2.3. First, in Section 2.2 the structure parameters ($C^2_{n,\lambda}$,C^2_T,C^2_q, C_{Tq}) used in the processing are explained.

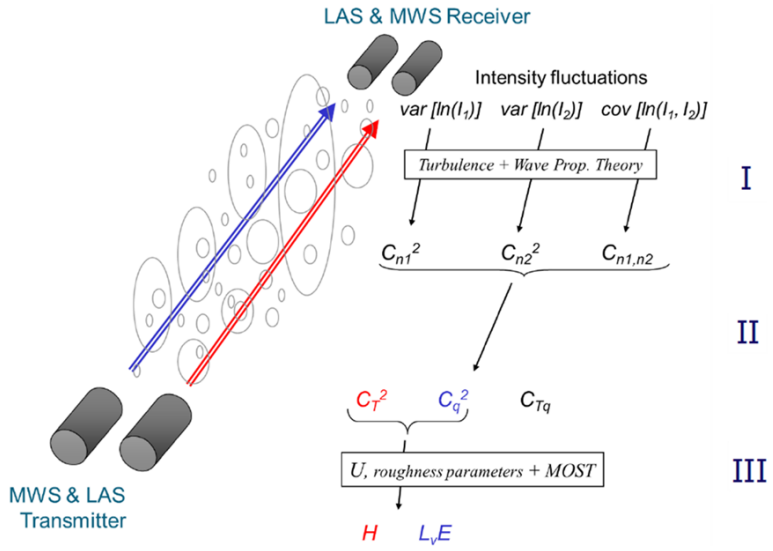

Figure 1: *Measurement principle of combined optical-microwave scintillometers, together with the subsequent processing steps to calculate the fluxes when applying the bichromatic method described by Lüdi et al. (2005)*

2.2 Structure parameters

In the processing steps indicated in Figure 1, structure parameters ($C^2_{n,\lambda}$,C^2_T,C^2_q, C_{Tq}) are used to eventually derive the surface fluxes. They can be seen as a statistical measure of the turbulent energy present in the inertial sub-range of the refractive index (n), temperature (T), and specific humidity (q) turbulence spectra[3]. The inertial sub-range is that part of the spectrum where the turbulent energy is only transported towards smaller spatial scales: no production or dissipation occurs. At larger spatial scales turbulent energy is produced (referred to as the production range), while at smaller spatial scales turbulent energy is dissipated (referred to as the dissipation range).

As argued by Braam (2014), in general the inertial sub-range comprises the spatial scales where both the optical and microwave scintillometer are most sensitive. In this range the spectra are directly proportional to the structure parameter. The three-dimensional turbulent spectrum of the refractive index for instance is defined as (based on the theory of Kolmogorov (1941)):

$$\phi_n(K) = 0.033 C^2_{n,\lambda} K^{-11/3}, \tag{1}$$

[3] To be more precise, it should be noted that $C^2_{n,\lambda}$ also depends on the wavelength (λ) of the considered scintillometer, and that C_{Tq} is actually derived from the co-spectrum of temperature and specific humidity.

where K is the three-dimensional wavenumber. From the equation above, it follows that $C_{n,\lambda}^2$ determines the magnitude of ϕ_n for a given range of K. Hence, the structure parameters are proportional to the total amount of turbulent energy in the inertial sub-range.

Furthermore, the structure parameters are related to the so-called structure function D_{a^2}, where a is a certain scalar (Moene et al., 2004). This structure function is a measure of the variance associated with fluctuations of the scalar a at a spatial range determined by the separation distance r. For instance for the refractive index n, in the inertial sub-range the structure function can be described as (Tatarskii, 1961; Moene et al., 2004):

$$D_{n^2}(r) = \overline{(n(x+r) - n(x))^2} = C_{n,\lambda}^2 r^{2/3}, \tag{2}$$

where the overbar indicates a spatial average, x is a certain position in the atmospheric flow, and r corresponds to spatial scales within the inertial sub-range. This equation thus shows that the structure parameters are statistical variables directly proportional to the variance of turbulent fluctuations in the inertial sub-range.

In Section 2.3 the processing steps for optical-microwave scintillometers are described, which rely on the structure parameters explained in this section.

2.3 Processing raw data from optical-microwave scintillometers to fluxes

In this section, the three consecutive processing steps to determine eventually the surface fluxes (Figure 1) will be briefly explained. The explanation focuses on the processing steps required for the optical-microwave scintillometers that will be investigated in this research.

2.3.1 Step I: from intensity fluctuations to $C_{n,\lambda}^2$

The first processing step is to calculate the structure parameters of the refractive index for both the optical ($C_{n,opt}^2$ $[m^{-2/3}]$) and microwave scintillometer ($C_{n,mw}^2$ $[m^{-2/3}]$) from the log-intensity fluctuations at the receiver (expressed as variances). Furthermore, in case the bichromatic method described by Lüdi et al. (2005) is applied, the covariance between the optical and microwave scintillometer signals is used to calculate an additional combined structure parameter ($C_{n,opt,mw}$ $[m^{-2/3}]$).

The relation between the log-intensity fluctuations and $C_{n,\lambda}^2$ can be expressed via a theoretical model that considers turbulence and wave propagation characteristics[4], integrated over all the relevant turbulence scales and the path length between the transmitter and receiver (Lawrence et al., 1972). Assuming that the optical and microwave scintillometer are only sensitive to eddies in the inertial sub-range, the analytical solutions of this model for the optical and microwave scintillometer can be written as (Wang et al., 1978):

$$\sigma_{\ln(I),opt}^2 = c_{opt} D^{-7/3} L^3 C_{n,opt}^2, \tag{3}$$

$$\sigma_{\ln(I),mw}^2 = c_{mw} F^{-7/3} L^3 C_{n,mw}^2, \tag{4}$$

$$\sigma_{\ln(I),opt,mw} = c_{opt,mw} max(D,F)^{-7/3} L^3 C_{n,opt,mw}, \tag{5}$$

where c_{opt}, c_{mw}, and $c_{opt,mw}$ are constants $[-]$, L is the path length $[m]$, D is the diameter of the optical scintillometer $[m]$, F is the Fresnel length $[m]$ (defined as $F = \sqrt{\lambda L}$ with λ being the wavelength of the light beam $[m]$), and $max(D,F)$ indicates that only the maximum value of D and F is chosen. The analytical solutions for the optical and microwave scintillometer are very similar, except that $\sigma_{\ln(I),opt}^2$ scales with D, $\sigma_{\ln(I),mw}^2$ with F, and $\sigma_{\ln(I),opt,mw}$ with $max(D,F)$. This is related to the eddy scale for which the instrument is most sensitive: the signal of the optical scintillometer is most sensitive to eddies with a scale around D, while the signal of the microwave scintillometer is most sensitive to eddies with a scale around F (as long as the instrument is located high enough above the ground; Beyrich et al. (2012)). The covariance between the two signals, in turn, is mainly sensitive to eddies with scales corresponding to the maximum value of D and F.

2.3.2 Step II: from $C_{n,\lambda}^2$ to C_T^2 and C_q^2

After the structure parameters of the refractive index ($C_{n,opt}^2$ and $C_{n,mw}^2$) have been determined (Section 2.3.1), the next step is to determine the structure parameters of both temperature (C_T^2 $[K^2 m^{-2/3}]$) and humidity (C_q^2 $[\frac{kg}{kg}^2 m^{-2/3}]$). For this purpose, the structure parameters of the refractive index can be expressed as follows (Hill, 1997, e.g.):

$$C_{n,\lambda}^2 = A_{t,\lambda}^2 \frac{C_T^2}{\bar{T}^2} + A_{q,\lambda}^2 \frac{C_q^2}{\bar{q}^2} + 2 A_{t,\lambda} A_{q,\lambda} \frac{C_{Tq}}{\bar{T}\bar{q}}, \tag{6}$$

[4] This includes the so-called finite aperture averaging terms from Ochs et al. (1976), which takes into account the finite size of the apertures used in the scintillometers.

where $A_{t,\lambda}$, $A_{q,\lambda}$ are dimensionless coefficients depending on the wavelength λ, pressure P $[Pa]$, temperature T $[K]$, and specific humidity q $[\frac{kg}{kg}]$. C_{Tq} is the structure parameter of the temperature-humidity covariance $[\frac{kg}{kg}Km^{-2/3}]$, and the bars indicate average values. The used expressions for $A_{t,\lambda}$, $A_{q,\lambda}$ are identical to the ones in Ward et al. (2013). Note that the dependency of $C_{n,\lambda}^2$ on wavelength is only retained by the dimensionless coefficients $A_{t,\lambda}$, $A_{q,\lambda}$: C_T^2, C_q^2 and C_{Tq} are independent from the considered wavelength.

Hence, by using Eq.(6) for both the optical and microwave scintillometer, a system of two equations (for $C_{n,opt}^2$ and $C_{n,mw}^2$) results with in total three unknowns (C_T^2,C_q^2, C_{Tq}). Hence, the system is undetermined. To solve this issue, two different methods are used.

2.3.2.1 Two-wavelength method described by Hill (1997)

The first method to solve the system of equations is the two-wavelength method described by Hill (1997), which prescribes a certain value for r_{Tq}. r_{Tq} is the correlation coefficient between temperature and humidity $[-]$, defined as:

$$r_{Tq} = \frac{C_{Tq}}{\sqrt{C_T^2 C_q^2}}, \tag{7}$$

When r_{Tq} is prescribed as +1 or -1, solving the system of equations following from Eq.(6) gives:

$$\begin{cases} C_T^2 = \left[A_{q,mw}^2 C_{n,opt}^2 + A_{q,opt}^2 C_{n,mw}^2 \right. \\ \left. + 2A_{q,opt}A_{q,mw} r_{Tq} \sqrt{C_{n,opt}^2 C_{n,mw}^2} \right] \frac{T^2}{\gamma^2}, & (8) \\ C_q^2 = \left[A_{t,mw}^2 C_{n,opt}^2 + A_{t,opt}^2 C_{n,mw}^2 \right. \\ \left. + 2A_{t,opt}A_{t,mw} r_{Tq} \sqrt{C_{n,opt}^2 C_{n,mw}^2} \right] \frac{q^2}{\gamma^2}, & (9) \\ C_{Tq} = r_{Tq} \sqrt{C_T^2 C_q^2}, & (10) \end{cases}$$

where $\gamma = A_{t,mw}^2 A_{q,opt}^2 - A_{t,opt}^2 A_{q,mw}^2$.

The assumption that r_{Tq} is equal to +1 or -1 should be true when the atmosphere strictly obeys Monin-Obukhov Similarity Theory (MOST; see Section 2.3.3) (Hill, 1989).

However, the assumptions behind MOST are often violated in reality. As a result, it appears that in practice r_{Tq} can better be described with values around 0.8 or even lower (Ward et al., 2015a).

The sign of r_{Tq}, in turn, should be equal to the combined signs of H and LE, which causes a sign-ambiguity in r_{Tq}: a positive r_{Tq} for instance can refer to cases where both H and LE are either positive or negative. Since LE is considered to be always positive, usually positive values are prescribed during daytime and negative values during night time: the sign of r_{Tq} is then only determined by the sign of H. This is accurate most of the time, but fails during dew fall-events ($LE < 0$) (Ward et al., 2015b).

2.3.2.2 Bichromatic method described by Lüdi et al. (2005)

The second method used to solve the system of equations is the bichromatic method described by Lüdi et al. (2005), which relies on the covariance between the optical and microwave scintillometer signals to derive an additional structure parameter ($C_{n,opt,mw}$). As a result a third equation enters the system of equations defined by Eq.(6), which gives:

$$\begin{cases} C_T^2 = \Big[A_{q,mw}^2 C_{n,opt}^2 + A_{q,opt}^2 C_{n,mw}^2 \\ \qquad - 2A_{q,opt}A_{q,mw}C_{n,opt,mw} \Big] \dfrac{T^2}{\gamma^2}, & (11) \\ C_q^2 = \Big[A_{t,mw}^2 C_{n,opt}^2 + A_{t,opt}^2 C_{n,mw}^2 \\ \qquad - 2A_{t,opt}A_{t,mw}C_{n,opt,mw} \Big] \dfrac{q^2}{\gamma^2}, & (12) \\ C_{Tq} = \Big[- A_{t,mw}A_{q,mw}C_{n,opt}^2 - A_{t,opt}A_{q,opt}C_{n,mw}^2 \\ \qquad + (A_{t,opt}A_{q,mw} + A_{t,mw}A_{q,opt})C_{n,opt,mw} \Big] \dfrac{Tq}{\gamma^2}. & (13) \end{cases}$$

The advantage of the bichromatic method is that no value has to be assumed for r_{Tq} to solve the system, which allows to assess the stability of the atmosphere and provides information about the extent to which MOST is violated. However, the disadvantage is that the bichromatic method is less robust than the two-wavelength method: physically unrealistic values of r_{Tq} ($|r_{Tq}| \geq 1$) and chaotic behaviour sometimes occur (Ward et al., 2015a). Furthermore, the sign-ambiguity in r_{Tq} present in the two-wavelength method still remains.

2.3.3 Step III: from C_T^2 and C_q^2 to H and LE

The final step is to calculate H and LE from the structure parameters of temperature and humidity (C_T^2 and C_q^2), which were determined in the second processing step (Section 2.3.2). For this purpose, a theoretical framework called Monin-Obukhov similarity theory (MOST; Monin and Obukhov (1954)) is used. The basic idea behind MOST is that quantities related to turbulence (gradients, variance, structure parameters), can be connected to turbulent fluxes via universal equations. In this context, universal means that the equations are equal for different atmospheric conditions. These universal equations are determined by fitting relationships between dimensionless groups of variables based on data from field experiments.

In literature different forms of the MOST-equations have been found, despite the assumption that the equations should be universal. According to Braam (2014), this is likely related to differences in data processing, instrumentation (including the measurement height), and surface characteristics (especially soil moisture and heterogeneity). In order to define more robust MOST functions, Kooijmans and Hartogensis (2016) therefore used data from eleven field experiments that were gathered with the same instrumentation and processed in the same way. They found that differences in the range of stabilities (unstable, stable) covered in the field experiments and a limited amount of available data are both plausible explanations for the discrepancies found in literature. By combining the data from all the field experiments, they defined the following general form of the MOST-equations:

$$f_{C_T^2,unstable} = 5.6(1 - 6.5\frac{z}{L_o})^{-2/3}, \tag{14}$$

$$f_{C_q^2,unstable} = 4.5(1 - 7.3\frac{z}{L_o})^{-2/3}, \tag{15}$$

$$f_{C_T^2,stable} = 5.5(1 + 1.1\frac{z}{L_o}^{2/3}), \tag{16}$$

$$f_{C_q^2,stable} = 4.5(1 + 1.1\frac{z}{L_o}^{2/3}), \tag{17}$$

where $\frac{z}{L_o}$ is a dimensionless height with L_o being the Obukhov length $[m]$. This can be seen as a measure for the atmospheric stability: negative values of $\frac{z}{L_o}$ indicate unstable conditions, positive values stable conditions, and values close to zero neutral conditions. Furthermore, $f_{C_T^2}$ and $f_{C_q^2}$ indicate dimensionless groups that can be expressed as follows:

$$f_{C_T^2} = \frac{\rho^2 c_p^2 u_*^2 z^{2/3} C_T^2}{H^2}, \tag{18}$$

$$f_{C_q^2} = \frac{\rho^2 L_v^2 u_*^2 z^{2/3} C_q^2}{(1-\bar{q}) LE^2}. \tag{19}$$

Here, ρ indicates the air density $[\frac{kg}{m^3}]$, c_p the specific heat capacity at constant pressure $[\frac{J}{kg*K}]$, L_v the latent heat of vaporisation $[\frac{J}{kg}]$, and u^* the friction velocity $[\frac{m}{s}]$.

If the definition of L_o and the flux-profile relationships prescribing u^* are provided, the surface fluxes H and LE can be calculated iteratively from the structure parameters C_T^2 and C_q^2 using Eq.(14)-(19). This concludes the third processing step required to determine H and LE from the intensity fluctuations of the received signal (see Figure 1). We investigated multiple open issues related to the three explained processing steps, which will be introduced in Section 3.

3 Research Questions

3.1 RQ1: Band-pass filtering

In this step an important issue is that not only the surface fluxes H and LE contribute to the intensity fluctuations measured at the received signal, especially at low and high frequencies. To illustrate this, for the optical scintillometer used in this study (see Section 4) in Figure 2 a theoretical spectrum is given of the intensity fluctuations measured at the receiver, while in figure 3 a corresponding real spectrum is shown. Indeed, compared to the theoretical spectrum the real spectrum shows unwanted contributions both at low and high frequencies. At low frequencies mainly absorption can contribute, while at high frequencies the signal becomes sensitive to electronic noise (van Dinther et al., 2013, e.g.).

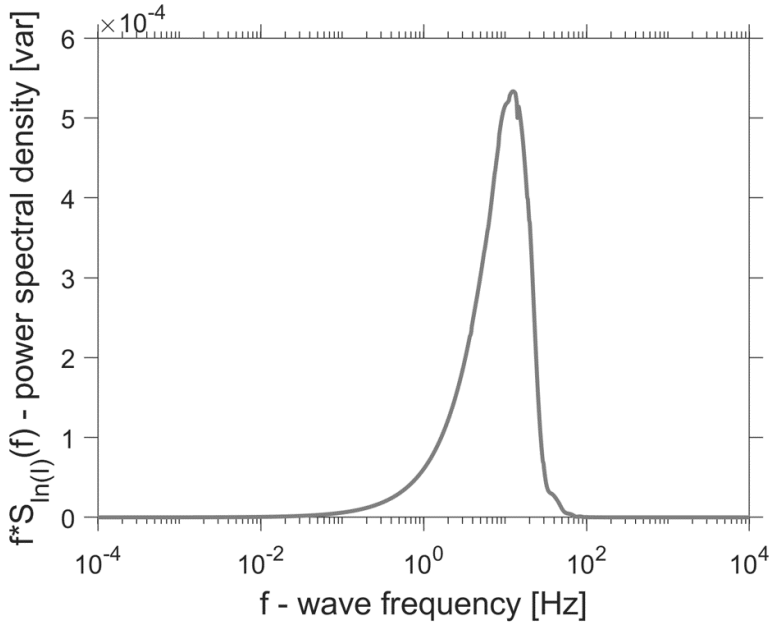

Figure 2: *Theoretical spectrum of the intensity fluctuations for the optical scintillometer considered in this study (see Section 4), as derived from the model of Clifford (1971) with* $U_{cross} = 3\ m/s$ *and* $C^2_{n,opt} = 5 * 10^{-16}\ m^{-2/3}$.

Therefore, in practise a band-pass filter (BPF) is applied to filter out these unwanted contributions to the raw scintillation signal. This includes a high-pass filter (HPF) and often also a low-pass filter (LPF) that are fixed at a certain frequency (Moene et al., 2005; Meijninger et al., 2006; Ward et al., 2015a, e.g.).

In that way, fluctuations associated with frequencies below the HPF and above the LPF are filtered out for all OMS data (Figure 3), and not taken into account in the calculation of $C^2_{n,\lambda}$.

The choice of a suitable fixed HPF and LPF is however not trivial: the filters have to remove as much as possible the unwanted contributions, but at the same time retain the contributions associated with the surface fluxes. On top of that, for a given scintillometer set-up[5] the cross-wind speed (the wind speed perpendicular to the scintillometer path) changes the frequency range at which the surface flux contributions are located: high cross-wind speeds cause a shift towards higher frequencies, while low cross-wind speeds cause a shift towards lower frequencies (van Dinther et al. (2013), e.g.; see Figure 6 and 7).

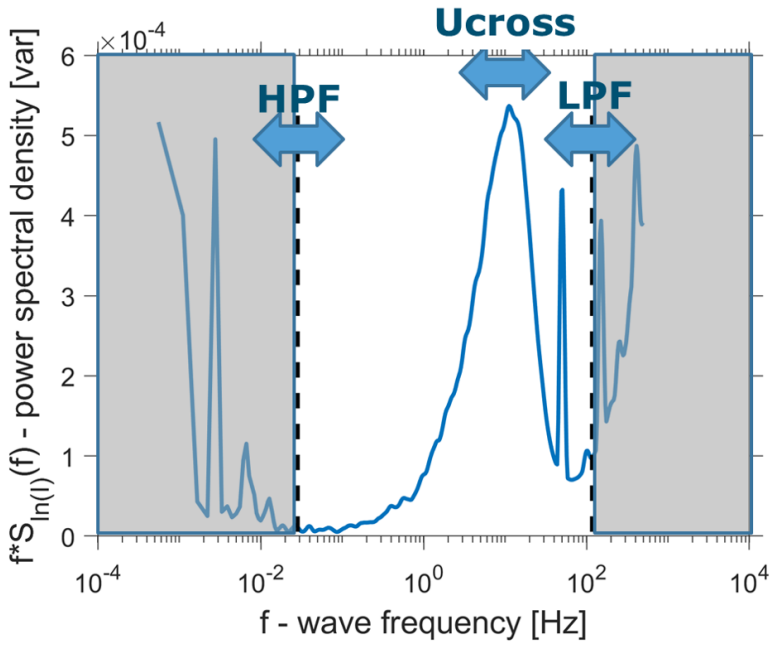

Figure 3: *Real measured spectrum of the intensity fluctuations for the optical scintillometer considered in this study (see Section 4). The commonly applied BPF is illustrated, which removes the unwanted contributions at low- and high-frequencies from the signal. Furthermore, the shift of the measured spectrum due to the cross-wind is indicated.*

[5]The scintillation spectrum changes also with D (in case of a Large Aperture Scintillometer (LAS)) or F (in case of a MicroWave Scintillometer (MWS)). While D is usually constant for different scintillometer set-ups with the same instrumentation, F does depend on the set-up considered because of the dependency on the path length (see also section 5.1.1.1; compare Figures 9a-10a to 9b-10b).

To tackle this issue, one study by Solignac et al. (2012) focused on properly removing absorption contributions from the signal measured by a near-infrared Large Aperture Scintillometer (LAS). Based on measurements from a 12-day period, they concluded that a fixed HPF of 0.2Hz should be preferred over HPFs of 0.1Hz or 0.5Hz. Furthermore, they showed that absorption substantially contributes to the measured $C^2_{n,opt}$ ($\sim 9\%$ on average).

So far, however, it has not been investigated yet what the most optimal fixed BPF is in a systematic way for both the LAS and MWS, taking into account the measured cross-wind regime, the characteristics of the measurement set-up (i.e. used wavelengths, aperture diameters, path length), and both low- and high-frequency unwanted contributions to the signal. Currently the HPF (and sometimes also LPF) are still often chosen based on experience and/or considering individual scintillometer spectra (such as in Figure 3), which may result in a BPF that is not optimal for the considered specific measurement set-up.

On top of that, erratic spikes present in the spectra (see for example Figure 3) are not always removed by the BPF. Those spikes are not associated with the surface fluxes, and therefore can deteriorate the quality of the fluxes calculated from the scintillometer measurements. Currently, however, there does not yet exist a filter for the scintillometers that properly removes these spikes in the spectra.

The first research question becomes:

1. What is the most optimal fixed[6] band-pass filter (BPF) to filter out unwanted contributions from the raw scintillation signal, taking into account the measured cross-wind regime, the characteristics of the measurement set-up, and a newly developed spike filter?

[6] Initially we investigated as well the performance of dynamic BPFs that shift along the frequency axis as function of the cross-wind speed, rather than using fixed filters (which was suggested by Solignac et al. (2012) and van Kesteren et al. (2015)). However, the dynamic filters did not show a clear improvement, which is why we now only focus on fixed filters. A weakness of dynamic filters is that they depend on accurate measurements of the cross-wind speed, which should be representative for the entire path length. In practice however, often only wind speed measurements are available at one or a few specific locations (as is the case in Lindenberg). This likely hampered the performance of the dynamic filters in our analysis.

3.2 RQ2: $C_{n,\lambda}^2$ minima

As explained in Section 2.3.2, in the second processing step Eq.(6) relates $C_{n,\lambda}^2$ to C_T^2, C_q^2 and C_{Tq}. This equation can be rewritten in terms of the Bowen ratio β and r_{Tq}[7] (see Appendix A), which implies that there should be an unique relationship between $C_{n,\lambda}^2$ and β for given values of r_{Tq}.

Interestingly, several papers found that $C_{n,mw}^2$ has a distinct minimum around $\beta \approx 2-3$. If it is assumed that $|r_{Tq}| = 1$, these papers showed that $C_{n,mw}^2$ should even be zero at the minimum (Leijnse et al., 2007; Ward et al., 2013). Such a minimum may reduce the sensitivity of the scintillometer to the surface fluxes H and LE: the measured $C_{n,mw}^2$ could become lower than the detection limit of the scintillometer, which would negatively affect the quality of the resultant fluxes.

So far however, to our knowledge the relationship between $C_{n,\lambda}^2$ and β for negative r_{Tq} and optical wavelengths has not been reported yet in literature. It is especially important to know if there are more minima than the one found in literature, and assess to what extent such minima can be found in experimental field data. We therefore aim to provide in this research a thorough description of the relationships between $C_{n,\lambda}^2$ and β that includes negative r_{Tq} and optical wavelengths. Furthermore, we assess the consequences for the quality of the measured fluxes by comparing the relationships predicted by theory to experimental field data.

The second research question is thus as follows:

2. How does $C_{n,\lambda}^2$ depend on the Bowen ratio and the correlation coefficient between temperature and humidity for both optical and microwave wavelengths, and what are the consequences of these relations for the practical usability of the optical-microwave scintillometers?

3.3 RQ3: Combined Lüdi-Hill method

In the bichromatic method described by Lüdi et al. (2005), as mentioned in Section 2.3.2 an important problem is that the derived values of r_{tq} often reach physically unrealistic values (i.e. $|r_{Tq}| \geq 1$) and show chaotic behaviour. In contrast, the two-wavelength method described by Hill (1997) prescribes r_{tq}.

[7] β is defined as the ratio between the surface fluxes H and LE (see Eq.(A.3)), and thus gives an indication whether temperature or humidity fluctuations dominate the signal. Furthermore, the sign of β tells whether the surface fluxes act in the same direction or not.

This has the advantage that the derived surface fluxes are more robust. We will therefore investigate whether the eventually resultant surface fluxes can be improved by combining the bichromatic method with the two-wavelength method. To this end, we will develop a new hybrid method that cleans the r_{Tq}-values derived from the bichromatic method and subsequently uses them in the more robust two-wavelength method. Hence, the third research question becomes:

3. Can the derived surface fluxes (H, LE) be improved by using cleaned r_{Tq}-values found with the bichromatic method described by Lüdi et al. (2005), as input for the two-wavelength method described by Hill (1997)?

4 Site and Data description

4.1 LITFASS datasets

For the first and third research question, we have used raw optical-microwave scintillometer (OMS) data from the meteorological observatory in Lindenberg (Eastern Germany) operated by the Deutsche wetterdienst (DWD). The observatory is surrounded by a heterogeneous environment consisting of patches with different types of land use (forest, grassland, agriculture, cities/villages), and modest changes in elevation (in the order of tens of meters). Noteworthy is that at this site multiple large field campaigns have been conducted which are referred to as LITFASS. More details about the site characteristics can be found in the papers describing these field campaigns (Beyrich et al., 2006, 2012, e.g.).

We used raw OMS data from May 2016 up to and including August 2016, so containing a large part of the growing season and summer. In this period accurate spatially-averaged measurements of H and LE are very relevant to for instance crop growth modelling and energy/water balance studies.

In this case, the considered OMS consisted of a near-infrared 940nm Large Aperture Scintillometer (LAS) developed by MAQ (Meteorology and Air Quality chair group, Wageningen University and Research, Wageningen, The Netherlands) with an aperture diameter of 15 cm, and a commercial 160GHz MicroWave Scintillometer (MWS) developed by MAQ and RPG (Radiometer Physic GmbH, Meckenheim, Germany) with an aperture diameter of 30 cm. The scintillometers were located at an effective height of approximately 45 meters, and measured with a frequency of 1000 Hz.

Furthermore, the path length between the transmitters and receivers was around 4.8 kilometres long. Figure 4 gives an overview of the path and instrumentation of the used OMS-system.

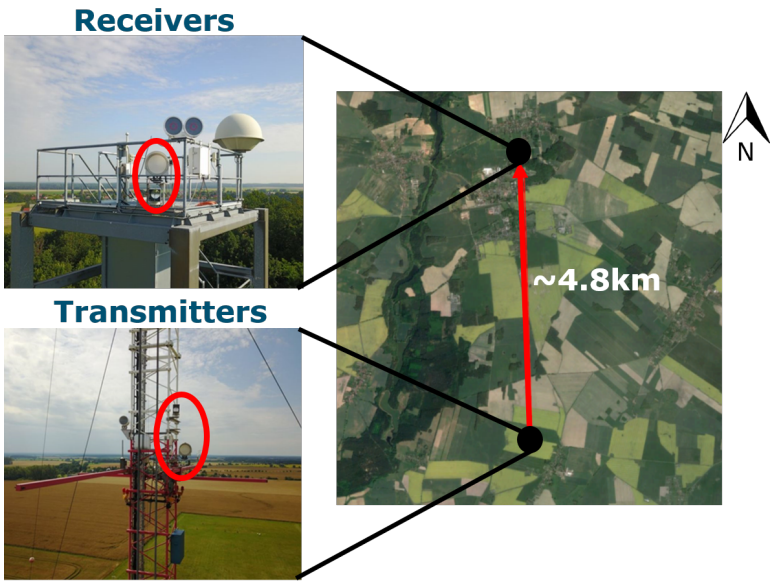

Figure 4: *The path and instruments of the OMS used in this research, which are located in the surrounding area of the meteorological observatory in Lindenberg (Eastern Germany).*

Besides that, we relied on eddy-covariance (EC) data. For the first and third research question, we used EC-data from the meteorological tower on which also the transmitters of the OMS were located (see Figure 4). The EC-measurements were taken at 50 meters height above the surface with a frequency of 20 Hz. Additionally, we obtained from the same meteorological tower auxiliary measurements of the pressure, temperature, humidity, and the wind speed.

For the second research question we used EC-data from two different field experiments during the LITFASS-2012 campaign, which included the required auxiliary measurements as well (i.e. pressure, temperature, humidity). These two field experiments consisted of an EC-system (measuring at 20 Hz) located a few meters above a colza and rye field. The data extended from May up to and including July 2012 (colza: 10 May - 25 July, rye: 11 May - 1 August). More details about the measurement set-up can be found in Kooijmans and Hartogensis (2016).

4.2 Pre-processing data

For the pre-processing of the OMS data used in the first research question, we divided the data into intervals of 30 minutes. This makes the calculated statistics (e.g. $C^2_{n,\lambda}$, r_{Tq}) and thus the eventually derived surface fluxes H and LE robust, while still allowing to assume that the fluxes are stationary within an interval. We normalized in each interval the measured intensities at the receiver with the average measured intensity of that interval, such that only the fluctuations of the signal were retained. Hereby, we removed data points where the measured intensity was below 5% or above 500% of the averaged measured intensity. We did not calculate anymore the statistics of an interval when more than 50% of the points were removed. The applied pre-processing of the OMS data used in the third research research question was very similar, except that we divided the data into 10-minute instead of 30-minute intervals.

For the pre-processing of the EC-data in the second research question though, we did use a data interval of 30 minutes. We derived for each interval C^2_T and C^2_q from the EC-data using nearly the same (strict) data processing procedure[8] as Kooijmans and Hartogensis (2016). After applying standard data treatments and corrections, in this procedure several criteria are used to select only the intervals in which the turbulent spectra have a clear inertial sub-range and MOST is approximately valid. As noted in Section 5.2.1, the presence of a clear inertial sub-range is required to calculate the structure parameters from the turbulent spectra. Please refer to Kooijmans and Hartogensis (2016) for a more detailed description of the criteria and all the applied processing steps.

For the EC-data used in the first research question, we followed a similar approach where we only implemented the criterion in Kooijmans and Hartogensis (2016) related to the presence of a clear inertial sub-range. We did this in order to retain as much intervals as possible, which allows a better comparison between EC and OMS data (see Section 5.1.1.3). Additionally, we removed intervals during which rainfall distorted the measurements.

[8] The only small difference is that we also filtered out intervals where $LE < 5\frac{W}{m^2}$. This has two main advantages: all negative Bowen ratios correspond to stable conditions (where $H < 0\frac{W}{m^2}$), and outliers with extreme high Bowen ratios (where $LE \approx 0\frac{W}{m^2}$) are removed. Furthermore, it should be noted that the description of the criteria in Kooijmans and Hartogensis (2016) contains an error: C^2_T, C^2_q scaled with $z^{2/3}$ should have a **minimum** value of $10^{-1.5}$ and 10^{-9} respectively.

5 Methodology and Results

In this section we will describe in detail the applied methodology and the results for each research question given in Section 3. A description of the used data can be found in Section 4.1.

5.1 RQ1: Band-pass filtering

5.1.1 RQ1: Methods

For the first research question we have compared the performance of different HPFs and LPFs in order to assess which BPF is most optimal (Section 3.1). To this end we first developed a new systematic way to choose the HPF and LPF based on the real part of the theoretical spectrum from Clifford (1971) (for an example see Figure 2), which considers the measured cross-wind regime, the scintillometers, and the path length between the transmitter and receiver (Section 5.1.1.1). Besides that, we implemented a new spike filter that removes erratic spikes directly from the LAS and MWS spectra (Section 5.1.1.2).

To illustrate the procedure used for the filters described above, we show in Figure 5 as an example one data interval from the MWS. In this case the BPF and spike filter work perfectly: they remove all unwanted contributions, but retain the signal associated with the surface fluxes. An important aspect is that the filtering is done based on a Fast Fourier Transform (FFT) of the signal, which has the important advantage that the actual cleaned signals of both the LAS and MWS can be calculated via an Inverse Fast Fourier Transfrom (IFFT). This is necessary to determine C_{Tq}[9], which depends upon the covariance between the cleaned signals of the LAS and MWS (i.e. $\sigma_{\ln(I),opt,mw}$).

[9] In the current research determining C_{Tq} is actually only necessary for the third research question. However, in practice C_{Tq} is needed to calculate C_T^2, C_q^2 in the second processing step when the bicrhomatic method from Lüdi et al. (2005) is used (Section 2.3.2).

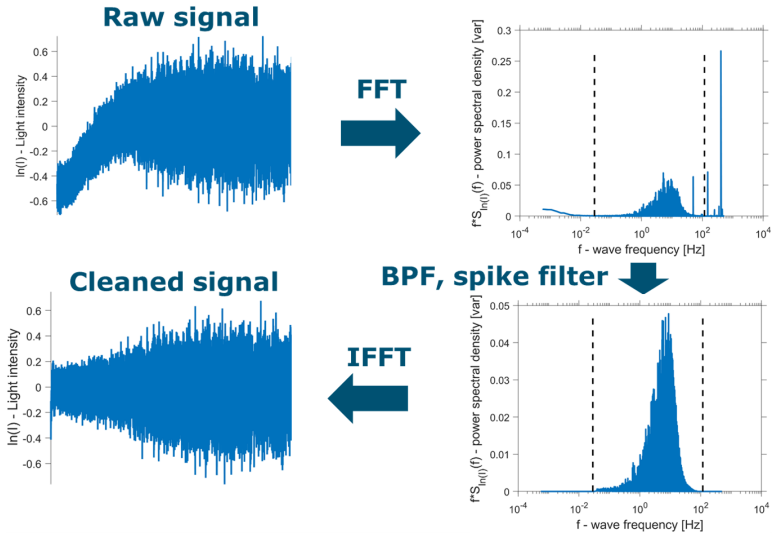

Figure 5: *Example data interval from the MWS, showing the used procedure to implement the BPF and spike filter. First, the raw signal is converted to a spectral representation via a Fast Fourier-Transform (FFT). Then, the spectral representation is utilized by the BPF and spike filter to remove unwanted contributions. After that, an Inverse Fast Fourier-Transform (IFFT) is applied to get the cleaned signal.*

Finally, for different combinations of HPFs and LPFs (chosen based on the procedure explained in Section 5.1.1.1) we validated the results by using EC-data as a reference (Section 5.1.1.3). Hereby, we included for all filter combinations already the spike filter. Excluding the spike filter did not substantially change the results of this comparison.

5.1.1.1 Choosing an appropriate BPF

As a first step to choose an appropriate BPF, for the LAS and MWS installed in Lindenberg (see Section 4.1) we defined a new criterion: the fraction of the variance that is retained for a certain BPF according to the real part of the theoretical spectrum from Clifford (1971), which takes into account the cross-wind speed and the characteristics of the measurement set-up. Since this theoretical spectrum does not consider unwanted contributions from for example absorption and electronic noise, the retained variance fraction indicates approximately how much of the variance associated with surface fluxes is retained. At the same time however, the unwanted contributions present in real measured spectra should be removed as much as possible.

There is thus a clear trade-off between the retaining the variance associated with the surface fluxes and removing unwanted contributions: the higher the theoretical retained variance fraction, the more likely it is that unwanted contributions to the signal are not removed.

In order to understand how this theoretical retained variance fraction can be used to determine an appropriate BPF, the first important consideration is that a certain prescribed theoretically retained variance fraction allows to determine a corresponding HPF and LPF: the HPF can be calculated by integrating the theoretical spectrum from high to low frequencies until the specified retained variance fraction is reached, while the LPF can be calculated in a similar way by integrating from low to high frequencies (Figure 6 and 7).

The second important consideration is the dependency of the theoretical spectrum on the cross-wind speed: as explained earlier the spectrum tends to shift towards higher frequencies for higher cross-wind speeds, although the shift becomes less pronounced when the cross-wind speed is high (Figure 6 and 7). Consequently, in order to ensure that not too much variance is removed at low or high cross-wind speeds, the HPF is based on the spectrum corresponding to the typical minimum cross-wind speed and the LPF on spectrum corresponding to the typical maximum cross-wind speed (Figure 6 and 7). If the cross-wind speed for the HPF is for instance chosen to be 8 m/s and the actual cross wind speed is below 8 m/s, more variance is removed than the chosen retained variance fraction suggests. Analogously, if the cross-wind speed for the LPF is chosen to be 8 m/s and the actual cross-wind is 15 m/s, too much variance is removed (Figure 6 and 7).

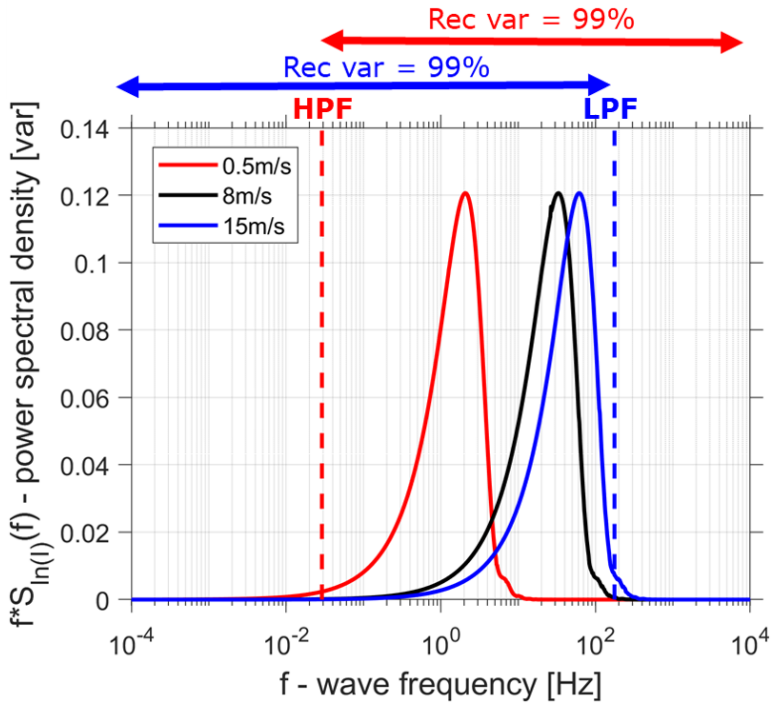

Figure 6: *Theoretical spectrum of the intensity fluctuations for the LAS used in this study (see Section 4.1) for three different cross-wind speeds, as derived from the model of Clifford (1971) with* $C^2_{n,opt} = 1 * 10^{-13}\ m^{-2/3}$. *As an example, the HPF and LPF corresponding to a retained variance fraction ("Rec var") of* 99% *are indicated.*

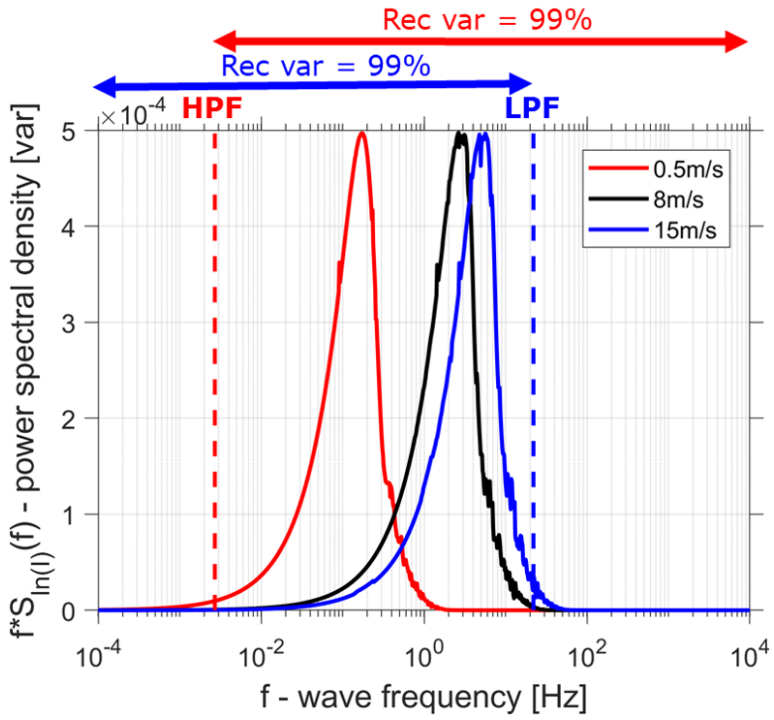

Figure 7: *Theoretical spectrum of the intensity fluctuations for the MWS used in this study (see Section 4.1) for three different cross-wind speeds, as derived from the model of Clifford (1971) with* $C^2_{n,mw} = 1 * 10^{-13}\ m^{-2/3}$. *As an example, the HPF and LPF corresponding to a retained variance fraction ("Rec var") of* 99% *are indicated.*

To assess what the typical minimum and maximum cross-wind speeds were for our raw OMS data (Section 4.1), we show in Figure 8 the measured cross-wind speeds in Lindenberg during the measurement period (May - September 2016). It appears that the cross-wind was only ∼5% of the time below 0.5 m/s and in general did not exceed 10-15 m/s (Figure 8). For this reason we assume that the typical minimum cross-wind speed in Lindenberg was around 0.5 m/s, and that the typical maximum cross-wind speed was, to be on the safe side, around 15 m/s.

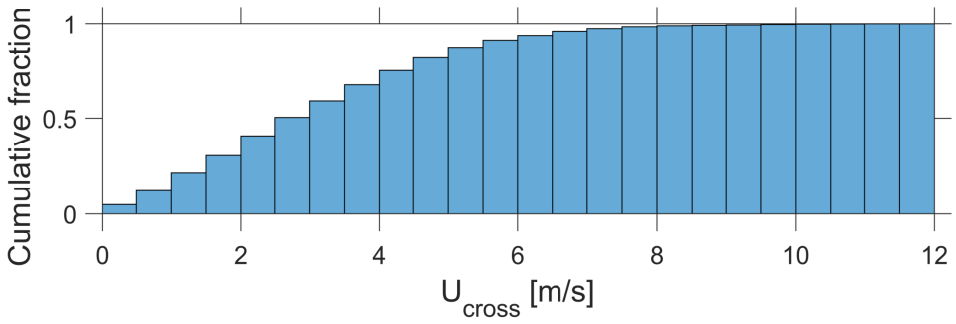

Figure 8: *Normalized cumulative histogram of the measured cross-wind speed at the meteorological observatory in Lindenberg from May 2016 up to and including August 2016.*

In short, for the LAS and MWS deployed in Lindenberg we can choose a LPF and HPF based on the path length (which is in Lindenberg fixed at 4.8 kilometers; see Section 4.1), the typical minimum/maximum cross-wind speeds (which are in this case 0.5 m/s and 15 m/s respectively), and a chosen theoretical retained variance fraction of the surface flux contributions (Figure 9 and 10). When a higher theoretically retained variance fraction is chosen, the corresponding HPF decreases while the corresponding LPF increases. In that way, less frequencies are filtered out and thus more variance is retained. Furthermore, it becomes apparent that both the HPF and LPF increase with cross-wind speed. As mentioned before the spectra shift towards higher frequencies when the cross-wind speed increases, and thus the HPF and LPF should shift towards higher frequencies as well. Finally, a striking feature is that for the LAS both the HPF and LPF are (almost) constant with path length, while for the MWS the HPF and LPF decrease with path length. This is related to the typical size of the eddies for which the scintillometer is sensitive: the aperture diameter D for the LAS and the Fresnell length F for the MWS. Since F depends on the path length of the measurement set-up, the typical size of the eddies for the MWS depends on the path length as well. This change in size affects the theoretical spectrum and thus the BPF determined for a given theoretically retained variance fraction.

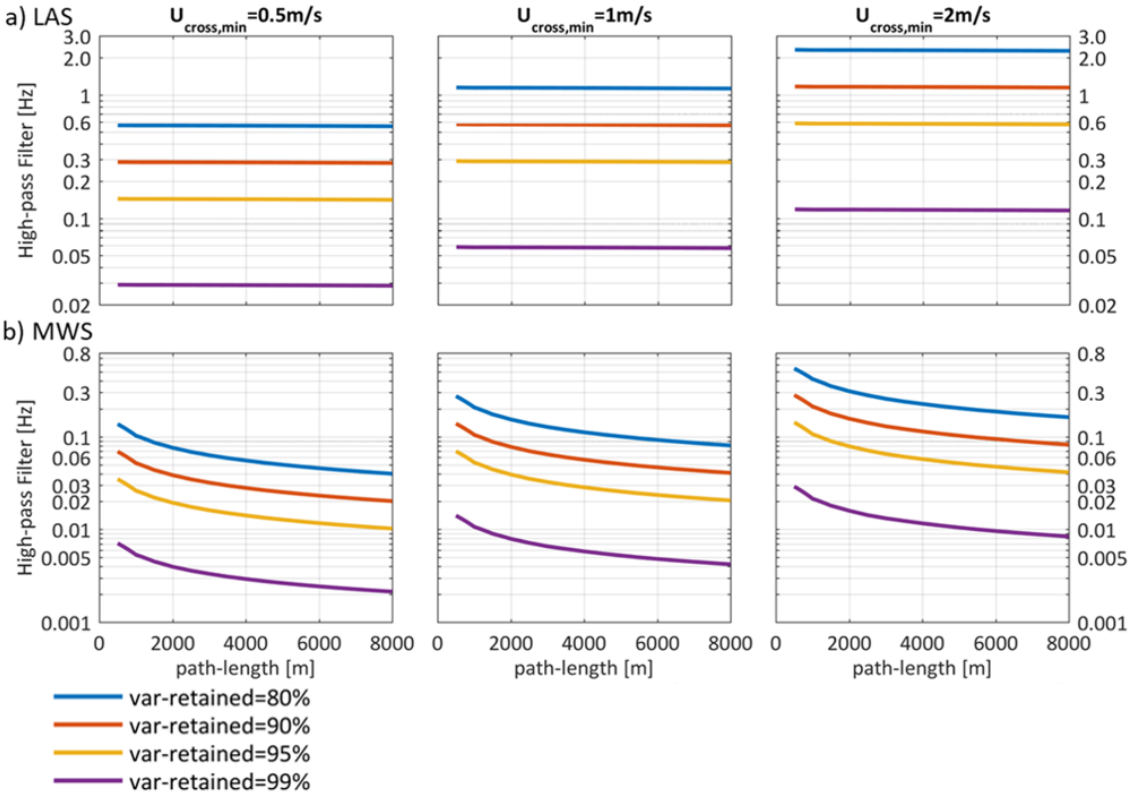

Figure 9: *Theoretical retained variance fraction as function of high-pass filter (HPF), cross-wind speed, and path length for the LAS (a) and MWS (b). Derived from the theoretical spectrum of Clifford (1971).*

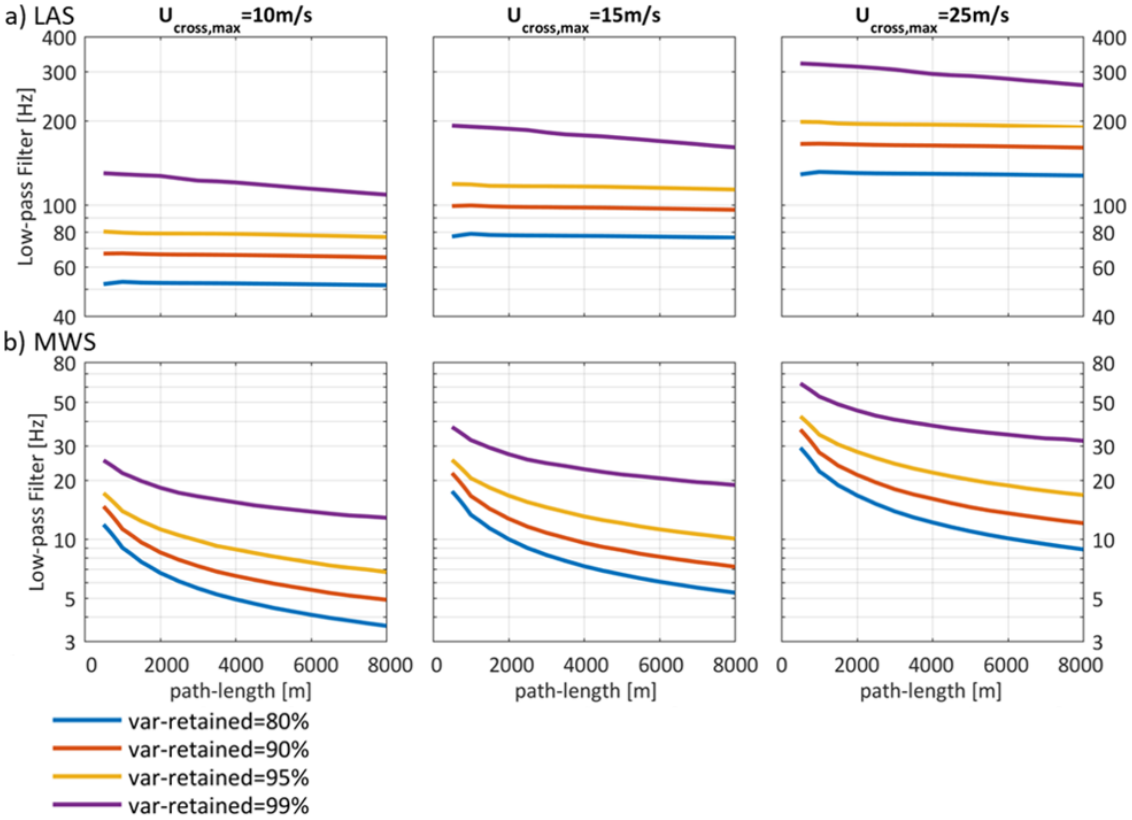

Figure 10: *Theoretical retained variance fraction as function of low-pass filter (LPF), cross-wind speed, and path length for the LAS (a) and MWS (b). Derived from the theoretical spectrum of Clifford (1971).*

In our research, we considered for the HPF three different theoretical retained variance fractions (90%, 95%, 99%) and for the LPF two different variance fractions (95%, 99%)[10]. For all possible combinations between these HPFs and LPFs, we assessed the performance by comparing the resulting log-values for $C^2_{n,mw}$ and $C^2_{n,opt}$ against the ones derived from EC-data (see also Section 5.1.1.3). Hereby, we considered as well the performance of combinations where the HPF and/or LPF were not included. For the LAS and MWS this adds up to 12 different filter combinations in total (see Table 1). This comparison allows us to investigate which of these filter combinations give the best performance.

[10]Based on a pre-analysis of individual spectra, it appeared that using lower variance fractions for the HPF and LPF already removed too much. Hence, in order to save computation time these lower variance fractions were already ruled out.

Table 1: *The different combinations of HPF and LPF used to assess which BPF is most optimal (see Section 5.1.1.3), for both the LAS and MWS. They were chosen based on the procedure explained in Section 5.1.1.1. 'frac' stands for the theoretical retained variance fraction, calculated using the real part of the theoretical spectrum from Clifford (1971).*

Combination	HPF			LPF		
	frac [%]	value MWS [Hz]	value LAS [Hz]	frac[%]	value MWS [Hz]	value LAS [Hz]
1	None	NA	NA	None	NA	NA
2				99	22	176
3				95	12	117
4	99	0.0027	0.029	None	NA	NA
5				99	22	176
6				95	12	117
7	95	0.013	0.14	None	NA	NA
8				99	22	176
9				95	12	117
10	90	0.026	0.28	None	NA	NA
11				99	22	176
12				95	12	117

5.1.1.2 Despiking OMS data

After the pre-processing described in Section 4.2, we applied a new developed spike filter to remove erratic spikes from the LAS and MWS spectra that are not related to surface fluxes. We will now describe the developed spike filter in more detail.

First of all, we apply a certain BPF (see Sections 3.1 and 5.1.1.1) prior to adopting the spike filter. Subsequently, the spikes are only removed in the part of the spectrum that is left. This saves computation time, especially when a LPF is implemented[11].

Hereby, these spikes are removed in blocks that extend along 5% of the width of the log(f) axis from the spectrum (as for instance the one in Figure 3). In each block, an iterative procedure is used to detect all the spikes based on the median of the absolute deviations (MADs) from the median. If a certain data point is located more than 10 MADs from the median within a block, it is classified as a spike. Then, this procedure is repeated until no more spikes are classified.

[11] At high frequencies more data points are present in the spectra than at low frequencies. Consequently, removing the highest frequencies with a LPF reduces considerably the time needed for the detection of all the spikes.

Furthermore, to ensure consistent results, overlap between the different blocks is implemented by shifting each time the block with a distance equal to 20% of the block width. On top of that, some smoothing is applied adjacent to the HPF and LPF by fitting a cosine[12]. This smoothing causes the filtered spectra to show slightly less abrupt transitions close to the HPF and LPF.

5.1.1.3 Validation against EC-data

Using the procedure described in Section 5.1.1.1, we have chosen in total 12 different filter combinations for both the LAS and MWS (see Table 1). In short, we will investigate their performance by comparing the log-values [13] of $C^2_{n,mw}$ and $C^2_{n,opt}$ to the ones calculated from EC-data.[14]. We do realize that there are systematic biases and uncertainties in this comparison. This makes statistical measures that are sensitive to biases, such as the root-mean square error, not suitable to evaluate the performance of the different filter combinations. For this reason, we relied instead on Pearson correlation coefficients to evaluate the performance of the different BPFs. Hereby, the main rationale is that a better BPF will reduce the scatter and thus increase the correlation coefficient.

In general, the comparison between the log-values of $C^2_{n,mw}$ and $C^2_{n,opt}$ derived from the OMS and EC-data was affected by several issues. Below we will present the most important ones, together with the way how we dealt with them:

1. Footprint differences between the OMS and EC-system, which cause scatter when comparing OMS- and EC-data (Hoedjes et al., 2007, e.g.). The OMS not only measures fluxes over a larger area than the EC-system, but also looks at a different area (see for instance Figure 11). Since these differences between the footprints are largest during night-time/stable conditions, we only considered daytime/unstable conditions (where $H > 5$ and $LE > 5 W m^{-2}$). During such conditions the land-uses present in both footprints are to some extent similar, allowing still to compare the OMS and EC-data on a general level.

[12] In case of the HPF this is done to a block with a width equal to 5% of the log(f) axis from the spectrum, while for the LPF this is done to a block with a width equal to 10% of the log(f) axis.

[13] The reasons to consider the log-transform rather than the values themselves are: 1) the C^2_n-values are approximately log-normally distributed, 2) the influence of a few severe outliers needs to be reduced, and 3) errors in low and high C^2_n-values should have approximately the same weight.

[14] We decided not to compare the eventual surface fluxes, because additional uncertainties introduced in the second and third processing step affect the performance as well. As a result, it becomes harder to distinguish the effects from the different filter combinations.

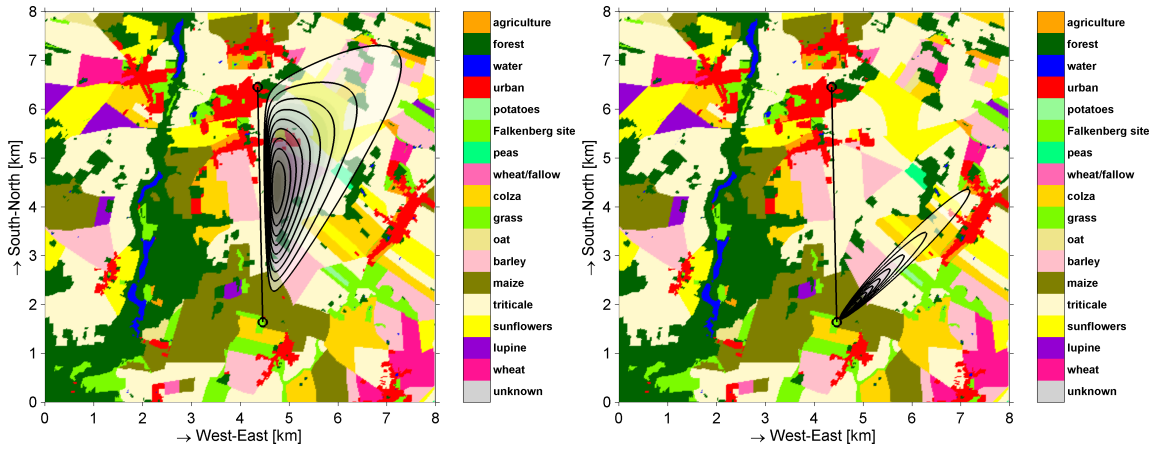

(a) LAS *(b) EC*

Figure 11: *The calculated footprint for the LAS and EC-system located in Lindenberg when the wind is coming from the North-east during daytime, unstable conditions. The colours indicate the land-uses as determined during the LITFASS-2009 field campaign.*

2. The substantial elevation of both the OMS and EC-system above the surface (45-50m), causing them to be located above the stable boundary layer during night-time conditions. Under these conditions thus decoupling occurs between the surface and the layer where the fluxes are measured, violating the assumptions behind the MOST-relationships. This is another reason why we only considered daytime, unstable conditions in our analysis.

3. Height difference between the OMS (effective height of 45 m) and the EC-system (height of 50 m). Since $C^2_{n,mw}$ and $C^2_{n,opt}$ depend strongly on height, this difference needs to be taken into account. In our analysis we will therefore multiply the C^2_n-values with $z^{2/3}$, which is a first-order correction strictly valid only under neutral conditions. For a more thorough correction the stability and the MOST-relationship need to be included, but this would introduce additional uncertainty that hampers the comparison between the OMS- and EC-data.

4. Saturation of the LAS during the day. This means that refractive index fluctuations associated with H become too strong, and consequently the underlying theory that connects the intensity fluctuations to the structure parameters does not hold anymore (Kohsiek et al., 2006).

When saturation occurs, the LAS will as a result underestimate the 'true' H. For this reason, we excluded the saturation regime from the LAS in our analysis[15].

As a final remark, we note that we included for all band-pass filter combinations the spike filter described in Section 5.1.1.2. This already removes some of the unwanted contributions. However, removing the spike filter did not change the outcome of the analysis (not shown).

5.1.2 RQ1: Results

In this section, we will first show the impact of the BPF and spike filter on the calculated variances (Section 5.1.2.1). Subsequently, we will compare the $log(C^2_{n,opt} * z^{2/3})$- and $log(C^2_{n,mw} * z^{2/3})$-values calculated from the raw OMS data using different filter combinations to the ones derived from EC-data (Section 5.1.1.1, 5.1.2.2).

5.1.2.1 Impact BPF and spike filter

Focusing first on the impact of a HPF, it becomes apparent that the applied HPF removes a considerable amount of variance from both the MWS-signal (in some cases even almost 100%) and LAS-signal (typically 0-10%) (Figures 12a and 13a). Less variance is removed though from the LAS-signal than from the MWS-signal, which seems to indicate that the MWS is more affected by low-frequency contributions (i.e. absorption) than the LAS.

When subsequently a LPF and spike filter are implemented, for both the MWS and LAS some additional variance is removed (typically 0-5%; Figures 12b-12c,13b-13c). Although the HPF removes more variance, the impact of the LPF and spike filter on the calculated variances can thus still be substantial.

[15] To be precise, we defined here the saturation regime as the points where the height corrected log-transform $log(C^2_{n,opt} * z^{2/3})$ of the EC-data is larger than -13 (see Figures 15c-15f).

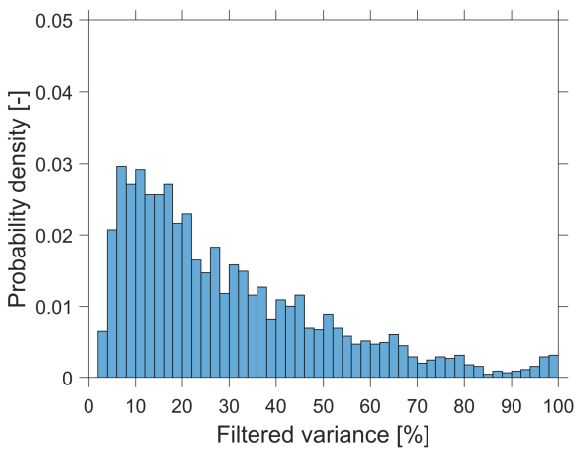

(a) Impact strict HPF (90% retained variance for a cross-wind speed of 0.5m/s)

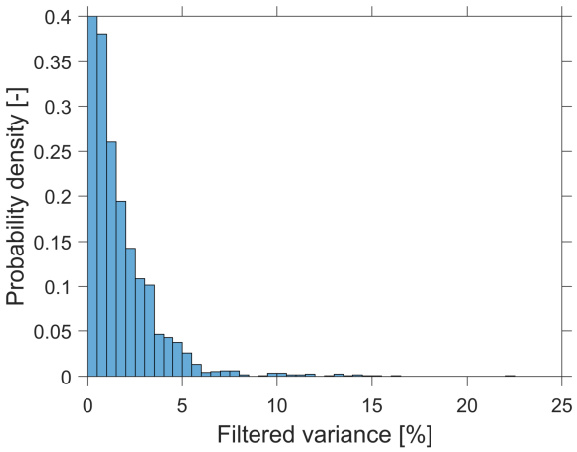

(b) Impact strict LPF (95% retained variance for a cross-wind speed of 15 m/s) w.r.t panel (a)

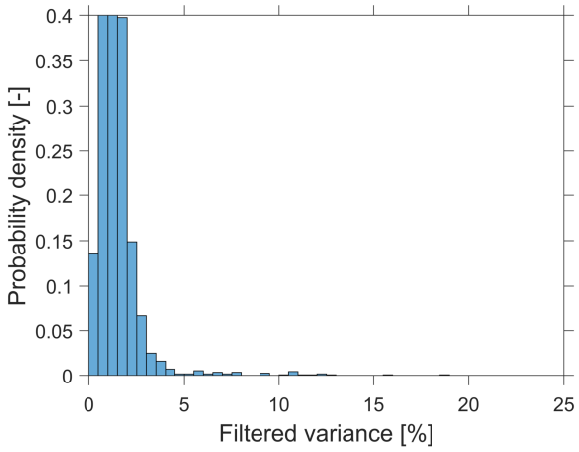

(c) Impact spike filter w.r.t panel (b)

Figure 12: *Histograms of the variance filtered from the MWS-signal (in %) by sequential application of a HPF (a), LPF (b), and spike filter (c). Only the intervals not removed by the filters discussed in Sections 4.2 and 5.1.1.3 are included. The percentages indicate how much of the variance from the theoretical spectrum calculated of Clifford (1971) is retained (see Section 5.1.1.1).*

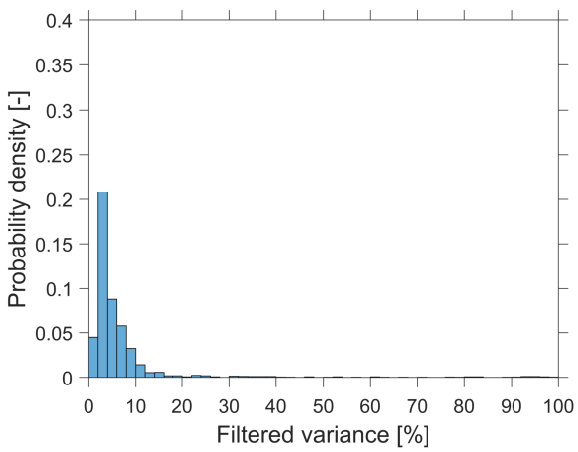

(a) Impact strict HPF (90% retained variance for a cross-wind speed of 0.5m/s)

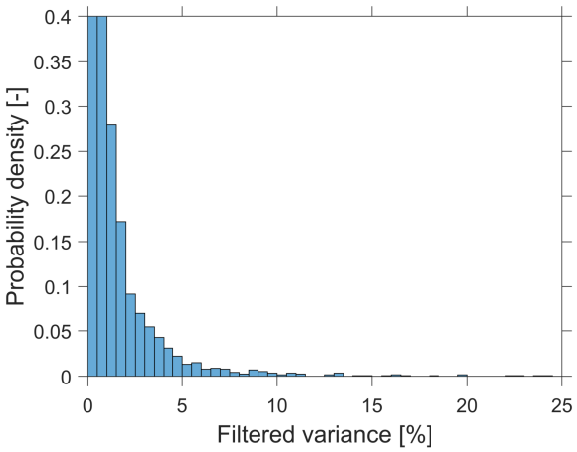

(b) Impact strict LPF (95% retained variance for a cross-wind speed of 15 m/s) w.r.t panel (a)

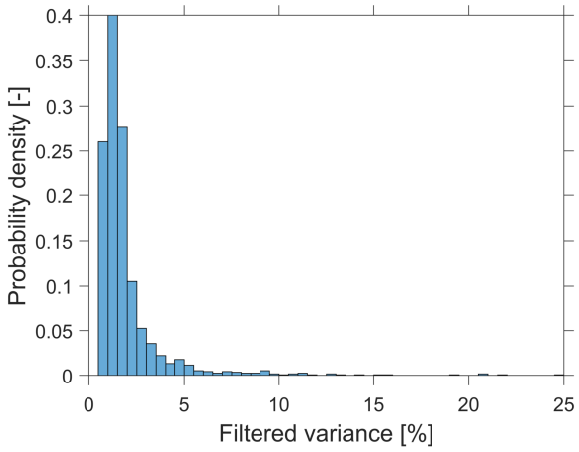

(c) Impact spike filter w.r.t panel (b)

Figure 13: *Histograms of the variance filtered from the LAS-signal (in %) by sequential application of a HPF (a), LPF (b), and spike filter (c). Only the intervals not removed by the filters discussed in Sections 4.2 and 5.1.1.3 are included. The percentages indicate how much of the variance from the theoretical spectrum calculated of Clifford (1971) is retained (see Section 5.1.1.1).*

5.1.2.2 Validation against EC-data

MWS

Comparing the $log(C^2_{n,mw}z^{2/3})$-values calculated from the MWS and EC-data for different filter combinations (Figure 14a and 14b), it is striking that the correlation coefficients are clearly lower when no HPF is included. Since a better BPF should reduce the scatter and thus result in a higher correlation coefficient (see Section 5.1.1.3), this is a good indication that a HPF improves the accuracy of the method. Besides that, the correlation coefficients suggest that including a strict HPF is more beneficial (where only 90% of the theoretical variance is retained with a cross-wind speed of 0.5m/s, and thus most unwanted contributions are removed) than including a loose HPF (where 99% of the theoretical variance is retained with a cross-wind speed of 0.5m/s, and thus possibly not all unwanted contributions are removed). In contrast, implementing a LPF does not have a clear effect on the calculated correlation coefficients: for a given HPF all the correlation coefficients are the same for different LPF. Hereby, the intervals where the BPF has the strongest effect (>10% variance removed by filter combination 12 in Table 1, the most strict BPF implemented;Figure 14a) show similar patterns as the other intervals (Figure 14b).

Focusing on individual scatter plots for some of the filter combinations (Figure 14c-14f), we see that the differences in correlation coefficients mainly reflect the amount of scatter present in the comparison, and not (systematic) biases between the methods. As explained in Section 5.1.1.3, we rely on correlation coefficients to ensure that (systematic) biases not related to the performance of the filters (most notably footprint/height differences) have no large impact on the comparison[16].

Clearly, the combination where no HPF is implemented shows much more scatter (Figure 14f) than the other scatter plots, confirming that implementing a HPF increases the correlation coefficient and likely improves the performance of the method. Furthermore, as reflected by the correlation coefficients, the combination with a strict HPF (Figure 14c) has slightly more scatter than the combination with a loose HPF (Figure 14e).

[16] In fact, the scatter plots (Figures 14c-14f) indeed indicate a systematic bias. The intervals corresponding with high available energies Q show systematically lower values for the MWS than for the EC-data. Our hypothesis is that this bias is caused by the height difference between the instruments: the correction we applied (see Section 5.1.1.3) is strictly only valid under neutral conditions, while these intervals mainly correspond to unstable conditions. This may have resulted in an underestimation of the $log(C^2_{n,mw}z^{2/3})$-values.

The scatter plot corresponding to a combination with both a HPF and LPF (Figure 14d), in turn, is almost identical to the plot corresponding with only the HPF (Figure 14c). Hence, the scatter plots confirm the patterns visible in the correlation coefficients.

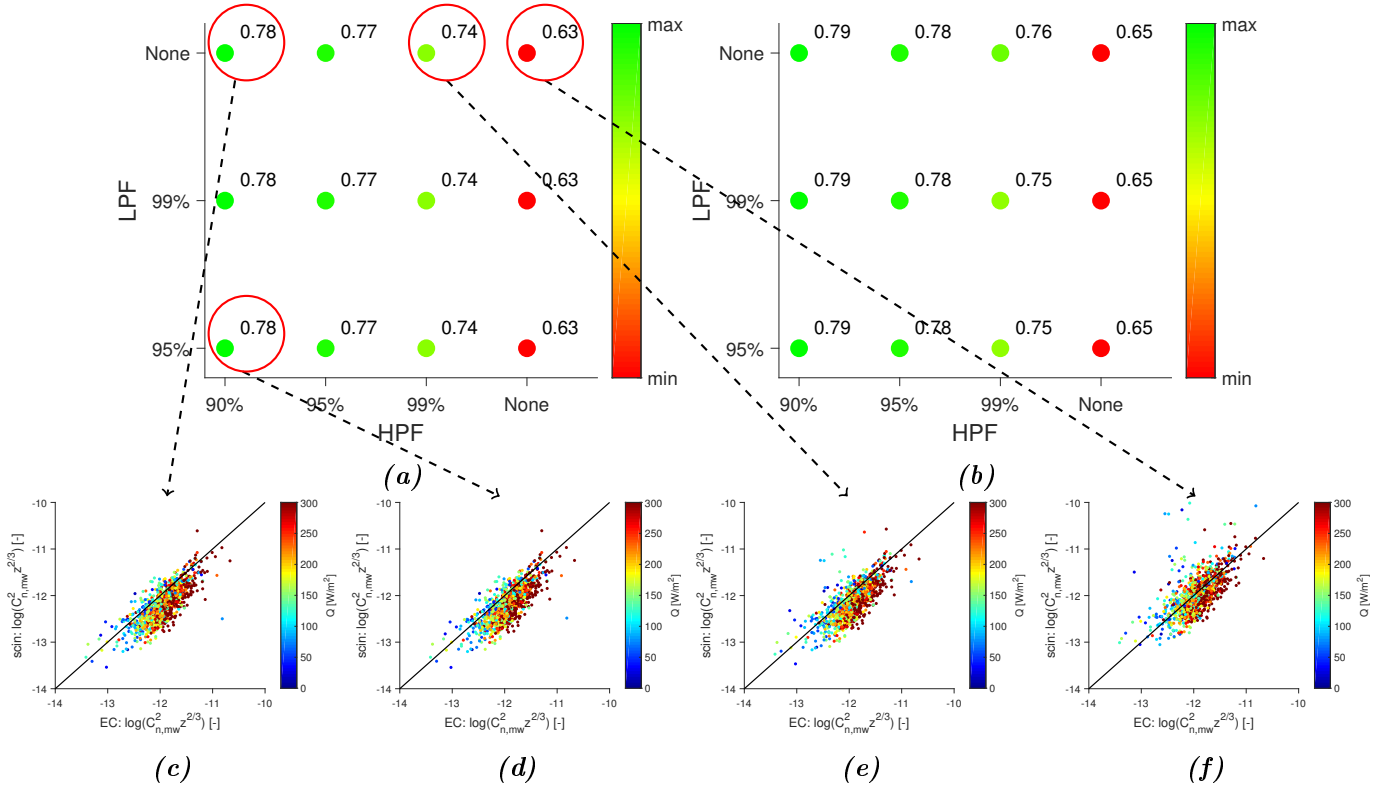

Figure 14: *Correlation coefficients between $log(C^2_{n,mw}z^{2/3})$ calculated from the MWS and EC-data, including only intervals where the most strict BPF considered (combination 12 in Table 1) removes at least 10% of the variance (a), or all intervals remaining after applying the filters mentioned in Sections 4.2 and 5.1.1.3 (b). Here, the colour scale shows for panel (a) and (b) separately which correlation coefficients are highest (green) and which ones are lowest (red). The percentages on the axes refer to the different LPFs and HPFs implemented, showing the theoretical retained variance for a typical minimum cross-wind speed of 0.5m/s (HPF) and a typical maximum cross-wind speed of 15m/s (LPF). Besides that, for four filter combinations shown in panel (a) the corresponding scatter-plots are given (c-f). In these plots the colour scale indicates the available energy Q (defined as $H + LE$). Note that for all shown filter combinations the spike filter described in Section 5.1.1.2 is already included.*

In short, based on Figure 14 we conclude that implementing a HPF is in general beneficial. Hereby, a strict HPF (where 90% of the theoretical variance is retained) seems to give a slightly better performance than a loose HPF (where 99% of the theoretical variance is retained). However, implementing a LPF has no clear effect. Considering the impact of the HPF and LPF on the calculated variances (Figure 12) this is not surprising: the HPF removes much more from the variance of the signal (up to 100%) than the LPF (up to 5-10%), making it easier to detect the effects of the HPF. Likely, the variability in the comparison between the MWS and EC-data is too large to detect the small effects of the LPF. Implementing a LPF is however still recommended: it does remove in some intervals unwanted contributions, and saves computation time when the spike filter is included (see Section 5.1.1.2).

LAS

Comparing the $log(C^2_{n,opt}z^{2/3})$-values calculated from the LAS and EC-data for different filter combinations (Figure 15a and 15b), similar as in Section 5.1.2.2 the correlation coefficients are much lower when no HPF is included. Besides that, in contrast to Section 5.1.2.2, it seems that using a loose HPF (where 99% of the theoretical variance is retained with a cross-wind speed of 0.5m/s) gives slightly better results than a strict HPF (where 90% of the theoretical variance is retained with a cross-wind speed of 0.5m/s). Remarkable is that implementing the LPF, in turn, reduces the correlation coefficient, suggesting that the LPF has a negative effect.

It is however important to note that the differences are clearly more pronounced for the intervals where the most strict BPF implemented (combination 12 in Table 1) removes at least 10% (Figure 15a). This is related to the modest impact of the BPF on the variance measured by the LAS: during most intervals the BPF does not remove much of the variance (<5-10%; Figure 13), and consequently has no large influence on the calculated correlation coefficients. Therefore, the differences between the filter combinations for the LAS become more clear when only the intervals are selected during which the BPF has a substantial impact.

Taking a closer look for some of the filter combinations at the corresponding scatter plots[17] (Figure 15c-15f), we see consistent with this that much less intervals are included since only some of them are strongly affected by the BPF. Similar to Section 5.1.2.2, the correlation coefficients again reflect the differences in the amount of scatter.

[17] Note that the saturation regime (defined as the points where the EC-values are higher than -13) is indicated in the scatter plots, but not taken into account in the calculation of the correlation coefficients (see also Section 5.1.1.3).

The combination with no HPF shows the most scatter (Figure 15f), while the combination with a loose HPF (Figure 15e) shows in contrast the lowest amount of scatter.

Focusing on the indicated combination with both a HPF and LPF (Figure 15d) together with the corresponding combination without LPF (Figure 15c), it seems that implementing the LPF only affects a few intervals where the scintillometer values are already lower than the EC-values. Although this causes the correlation coefficient to decrease, it is not likely that the LPF actually has a negative effect: only a few data points affected, causing the statistics to be easily influenced by outliers. Furthermore, it is important to realise that for low values the comparison between the scintillometer and EC-data becomes most troublesome: the intervals with lower values typically occur during intervals with close to neutral conditions, where the footprint differences become more important. In the individual spectra corresponding to these points, the LPF did properly removed the unwanted contributions without removing too much from the spectra associated with the surface fluxes (not shown).

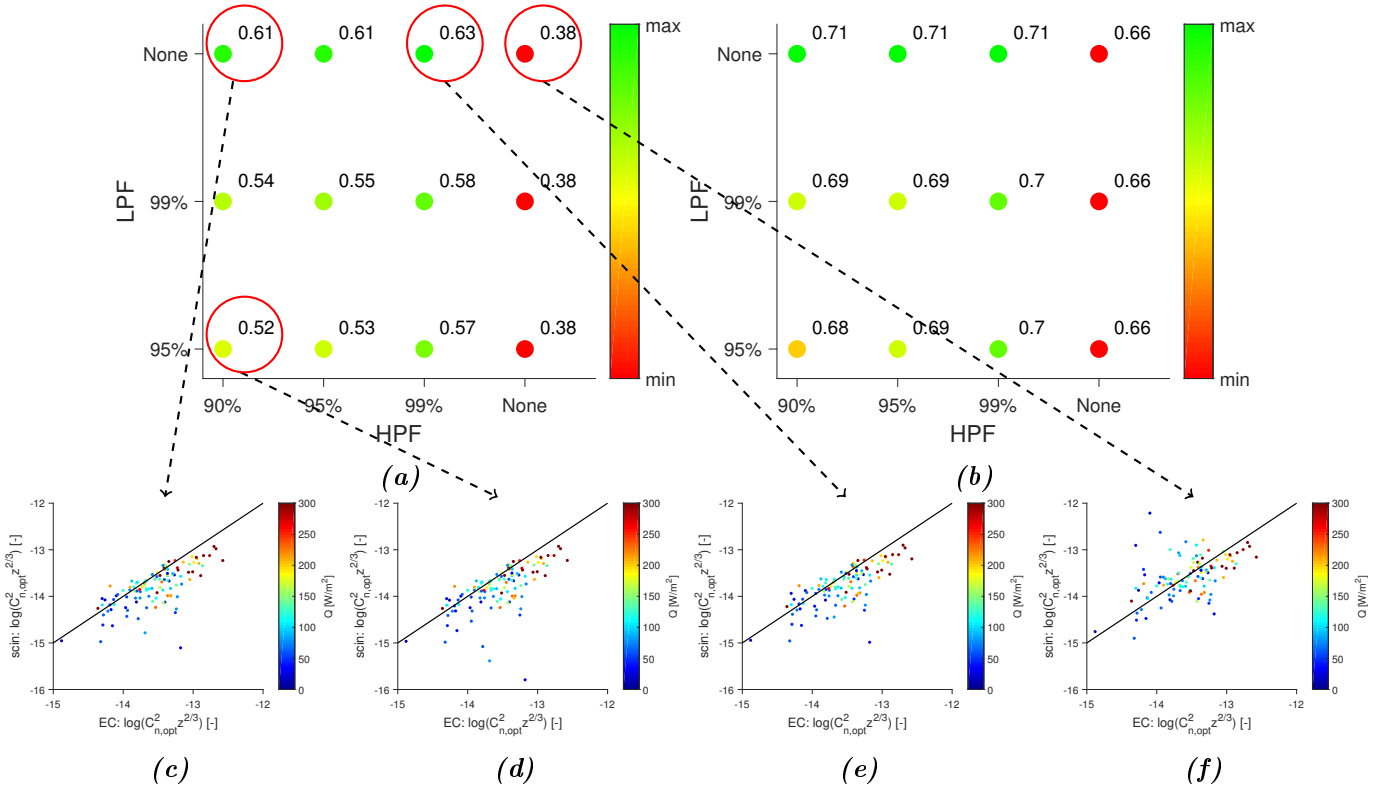

Figure 15: *Correlation coefficients between* $log(C^2_{n,opt}z^{2/3})$ *calculated from the LAS and EC-data, including only intervals where the most strict BPF considered (Combination 12 in Table 1) removes at least 10% of the variance (a), or all intervals remaining after applying the filters mentioned in Sections 4.2 and 5.1.1.3 (b). Here, the colour scale shows for panel (a) and (b) separately which correlation coefficients are highest (green) and which ones are lowest (red). The percentages on the axes refer to the different LPFs and HPFs implemented, showing the theoretical retained variance for a typical minimum cross-wind speed of 0.5m/s (HPF) and a typical maximum cross-wind speed of 15m/s (LPF). Besides that, for four filter combinations shown in panel (a) the corresponding scatter-plots are given (c-f). In these plots the colour scale indicates the available energy Q (defined as* $H + LE$*). Note that for all shown filter combinations the spike filter described in Section 5.1.1.2 is already included.*

Hence, based on Figure 15 we conclude that for the LAS implementing a loose HPF (where 90% of the theoretical variance is retained) seems to be most beneficial, while implementing a LPF does not seem to have a large impact on the performance of the method (despite that the correlation coefficients suggest otherwise). Still, for the same reasons as mentioned in Section 5.1.2.2, we recommend to include a LPF besides the HPF.

5.2 RQ2: $C_{n,\lambda}^2$ minima

5.2.1 RQ2: Methods

To investigate the research question posed in Section 3.2, we followed two different approaches: an analytical and an experimental one. For the analytical approach, we used Eq.(6) to derive and investigate thoroughly the relationships between $C_{n,\lambda}^2$ and β according to theory.

For the experimental approach we compared the found theoretical relationships to experimental EC-data, which allows us to assess the practical implications. We calculated the structure parameters (C_T^2, C_q^2, and C_{Tq}) from the turbulent power spectra of T and q measured by the EC-stations, where we retained only the structure parameters from intervals with a clearly defined inertial sub-range (using nearly the same criteria as Kooijmans and Hartogensis (2016), see Section 4.2). Similar to Kooijmans and Hartogensis (2016) these calculations relied on the MATLAB algorithms given in Hartogensis (2006), which are based on the relationships between C_T^2, C_q^2 and the turbulent power spectral densities of T, q in the inertial sub-range.

Subsequently, with the calculated C_T^2, C_q^2, and C_{Tq} we utilized Eq.(7) to determine r_{Tq} for each retained 30-minute interval. This allowed us, in turn, to calculate $\frac{C_{n,mw}^2}{C_T^2}$ and $\frac{C_{n,opt}^2}{C_T^2}$ via Eq. (20) relying on auxiliary measurements of pressure, temperature, and humidity[18] (see Section 4.1). Since we have measurements from the EC-data of both H and LE, the Bowen ratio could be easily determined as well. This enabled us to investigate the relationship between $\frac{C_{n,\lambda}^2}{C_T^2}$ and β for experimental EC-data, independent of the chosen method in the second processing step to solve for C_T^2, C_q^2, and C_{Tq}^2 (see Section 2.3.2). Furthermore, we were able to investigate the behaviour of the different terms in Eq. (6) as a function of β.

[18] Note that the difference between $\frac{C_{n,mw}^2}{C_T^2}$ and $\frac{C_{n,opt}^2}{C_T^2}$ is only due to the wavelength dependency of the dimensionless coefficients $A_{t,\lambda}$ and $A_{q,\lambda}$.

5.2.2 RQ2: Results

In this section, we first describe in full detail the analytical solution that connects $C_{n,\lambda}^2$ to β (Section 5.2.2.1). This includes the discovery of a new second theoretical minimum for $C_{n,opt}^2$. Next, we show how $C_{n,\lambda}^2$ derived from experimental EC-data (for description see Section 4.1) depends on β, which allows us to assess whether the found theoretical relationships and the two theoretical minima can also be observed in experimental EC-data. Finally, to complete the discussion we will present a thorough explanation for the occurrence of the two minima (Section 5.2.2.3).

5.2.2.1 Analytical approach

To complement the analytical results shown in literature (see Section 3.2), we first derived the following equation that connects $C_{n,\lambda}^2$ with β (for the full derivation including the made assumptions, see Appendix A):

$$\frac{C_{n,\lambda}^2}{C_T^2} = \underbrace{\frac{A_{t,\lambda}^2}{\overline{T}^2}}_{\text{Term A}} + \underbrace{\frac{A_{q,\lambda}^2}{\overline{q}^2}\frac{c_p^2}{L_v^2\beta^2}}_{\text{Term B}} + \underbrace{2|r_{Tq}|\frac{A_{t,\lambda}A_{q,\lambda}}{\overline{T}\,\overline{q}}\frac{c_p}{L_v\beta}}_{\text{Term C}}. \tag{20}$$

Note that only the ratio $\frac{C_{n,\lambda}^2}{C_T^2}$ can be prescribed based on β and r_{Tq}, rather than C_n^2 itself. It is not appropriate to assume a constant value for C_T^2 since C_T^2 also depends on β. This is not immediately apparent from the results shown in Leijnse et al. (2007) and Ward et al. (2013), which prescribe additionally the total available energy to calculate C_n^2 directly (see Appendix A for an alternative formulation of Eq.(20) based on Q). However, in doing so the results they show are only valid for the available energies they prescribed. The results from Eq.(20) are, in contrast, universal for all regimes of available energy. This allows a better comparison between the analytical solution and experimental data (see Section 5.2.2.2): the experimental data is continuously affected by changes in available energy.

Besides that, we found a straightforward analytical expression for the Bowen ratio at which $C_{n,\lambda}^2$ has a minimum, β_{min}, by setting the derivative of Eq.(20) with respect to β equal to 0:

$$\beta_{min} = -\frac{A_{q,\lambda}c_p\overline{T}}{A_{t,\lambda}L_v\overline{q}|r_{Tq}|}. \tag{21}$$

Next, we relied on Eq.(20) to calculate both $\frac{C_{n,mw}^2}{C_T^2}$ (Figure 16 and 18) and $\frac{C_{n,opt}^2}{C_T^2}$ (Figure 17) as a function of negative and positive β-values, using different values for r_{Tq}. Hereby, we assumed typical values for several atmospheric variables (Table 2).

Table 2: *The typical values used for calculating the results shown in Figures 16-18.*

Variable	Value [unit]
P	1000 $[hPa]$
T	288 $[K]$
q	0.010 $[\frac{kg}{kg}]$
L_v	$2.46 * 10^6$ $[\frac{J}{kg}]$
c_p	1005 $[\frac{J}{kg*K}]$

Consistent with Leijnse et al. (2007) and Ward et al. (2013) $\frac{C_{n,mw}^2}{C_T^2}$ shows a distinct minimum around $\beta \approx 2-3$. Also, as argued by Leijnse et al. (2007) the minimum in $\frac{C_{n,mw}^2}{C_T^2}$ becomes less apparent and shift towards larger β values when r_{Tq} decreases.

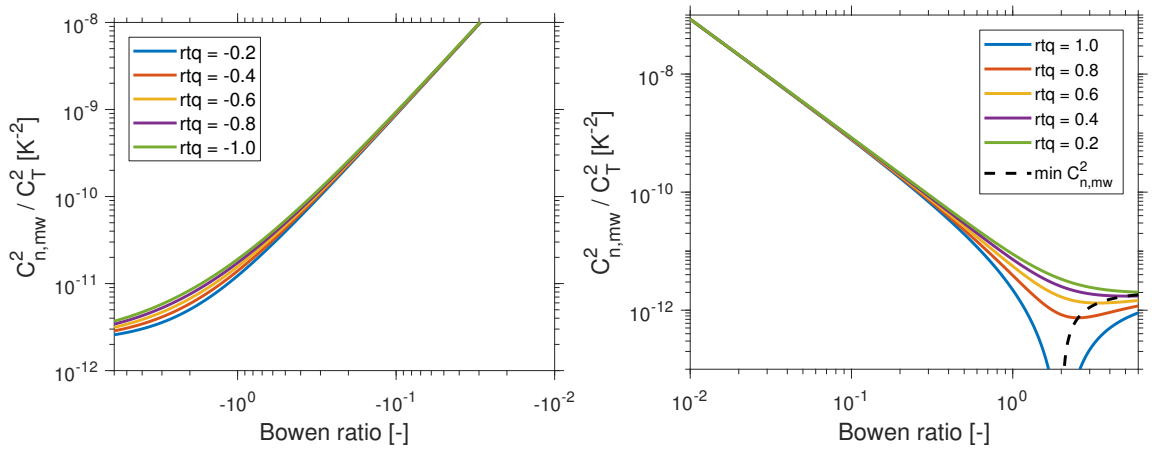

(a) *(b)*

Figure 16: *The structure parameter of the refractive index in the microwave region scaled with the structure parameter of temperature $[C^2_{n,mw}/C^2_T]$ versus negative (a) and positive (b) Bowen ratios $[\beta]$ according to Eq.*(20)*. The dotted line indicates the minima calculated with Eq.*(21)*. Hereby, we assumed typical atmospheric conditions (see Table 2). Note that both axes are logarithmic.*

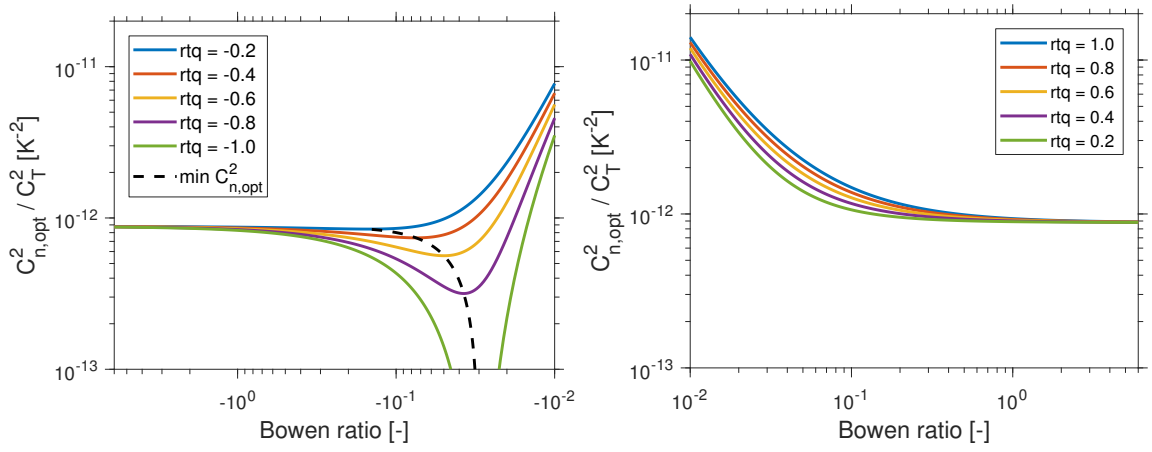

(a) *(b)*

Figure 17: *The structure parameter of the refractive index in the optical region scaled with the structure parameter of temperature $[C^2_{n,opt}/C^2_T]$ versus negative (a) and positive (b) Bowen ratios $[\beta]$ according to Eq.*(20)*. The dotted line indicates the minima calculated with Eq.*(21)*. Hereby, we assumed typical atmospheric conditions (see Table 2). Note that both axes are logarithmic.*

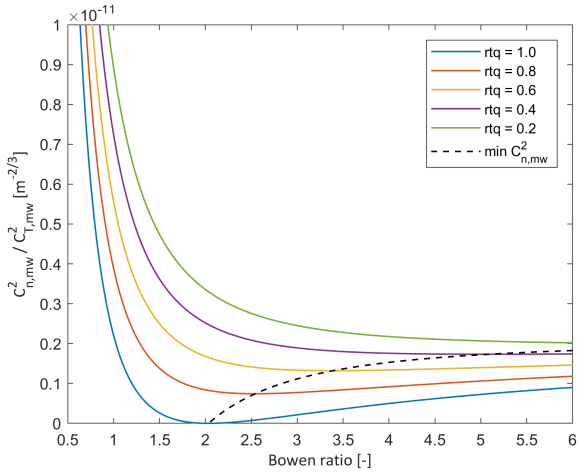

Figure 18: *The structure parameter of the refractive index in the microwave region scaled with the structure parameter of temperature* $[C^2_{n,mw}/C^2_T]$ *versus positive Bowen ratios* $[\beta]$ *according to Eq.*(20). *The dotted line indicates the minima calculated with* (21). *Hereby, we assumed typical atmospheric conditions (see Table 2). Note that the linear vertical and horizontal axes allow direct comparison with the results shown in Ward et al. (2013).*

Another noteworthy feature, not mentioned before in literature, is a minimum in $\frac{C^2_{n,opt}}{C^2_T}$ for negative β close to 0 (Figure 17a). Comparable to the minimum in $\frac{C^2_{n,mw}}{C^2_T}$, it becomes less pronounced and shifts towards more negative β when $|r_{Tq}|$ increases. In these two cases the minima arise because in Eq. (20) term C is negative, while the other two terms are positive. It appears that the decrease in magnitude of term B with increasing $|\beta|$ is offset by a decrease in magnitude of term C at larger $|\beta|$, causing a minimum in $\frac{C^2_{n,\lambda}}{C^2_T}$ (not shown). Since term C scales with $|r_{Tq}|$, this effect becomes less pronounced when the magnitude of $|r_{Tq}|$ decreases.

5.2.2.2 Experimental approach

To investigate whether the two theoretical minima (see Section 5.2.2.1) can be found in experimental field data, in Figure 19 and 20 $\frac{C^2_{n,mw}}{C^2_T}$ and $\frac{C^2_{n,opt}}{C^2_T}$ derived from EC-data of both a colza and rye field (see Section 4.1) are given as function of β. Furthermore, in Figure 21 the average $|r_{tq}|$ is shown together with the standard error for several bins. The bins are chosen such that they contain at least 10 data points.

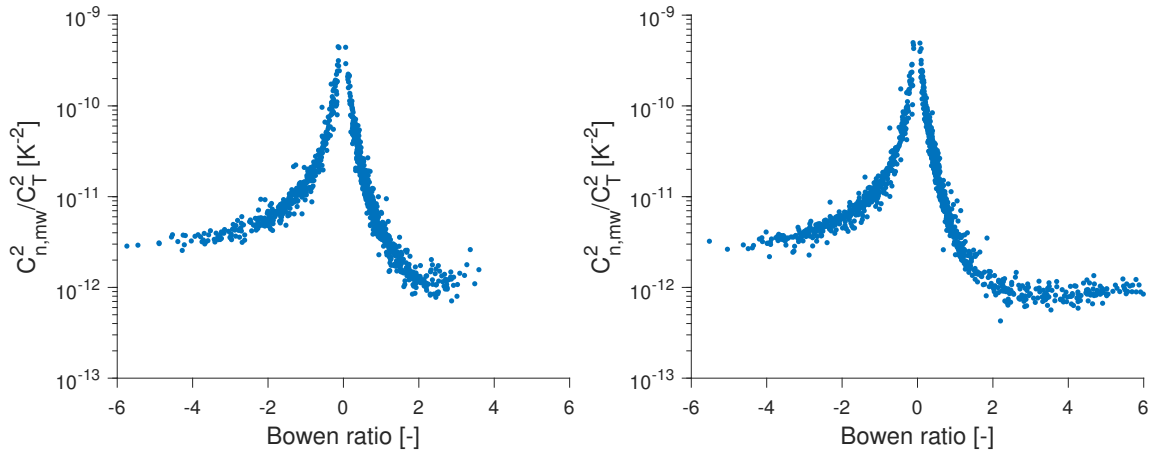

(a) Colza *(b) Rye*

Figure 19: *The structure parameter of the refractive index in the microwave region scaled with the structure parameter of temperature $[C^2_{n,mw}/C^2_T]$ versus negative (a) and positive (b) Bowen ratios $[\beta]$ as calculated from the EC-data described in Section 4.1.*

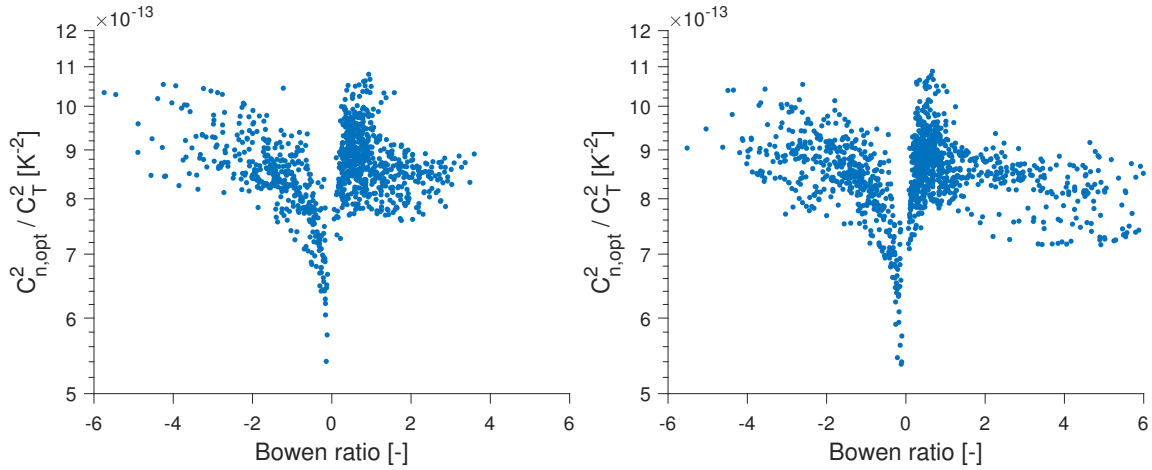

(a) Colza *(b) Rye*

Figure 20: *The structure parameter of the refractive index in the optical region scaled with the structure parameter of temperature $[C^2_{n,opt}/C^2_T]$ versus negative (a) and positive (b) Bowen ratios $[\beta]$ as calculated from the field data described in Section 4.1.*

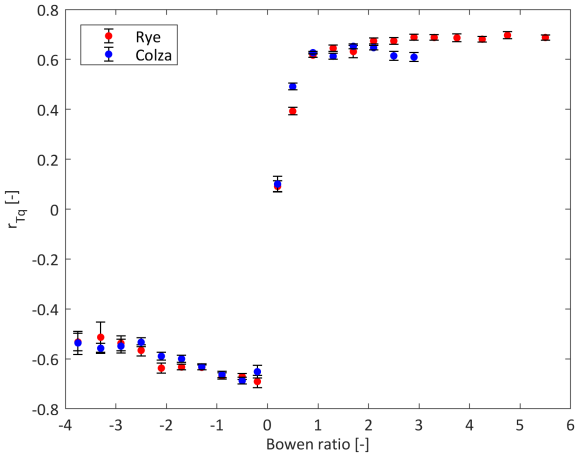

Figure 21: *The correlation coefficient between temperature and specific humidity [r_{Tq}] versus Bowen ratio [β] as calculated from the field data described in Section 4.1. Note that the field data has been divided into bins: for each bin the vertical black lines indicate the standard error.*

From Figures 19-21 it is clear that the patterns from the experimental field data agree reasonably well with the analytical solutions (Figures 16-18), considering that $|r_{Tq}|$ is around 0.5-0.7 for most Bowen ratios. As expected from the analytical solution, for $|r_{Tq}|$-values in this region the minima are visible but not very pronounced: $\frac{C_{n,mw}^2}{C_T^2}$ and $\frac{C_{n,opt}^2}{C_T^2}$ do not become equal to 0. This gives confidence in the ability of the analytical solution described in Section 5.2.2.1 to represent experimental field data.

Furthermore, Ward et al. (2015a) argued that in practice $C_{n,mw}^2$ would indeed not become equal to 0 because the measurements always contain some noise and thus the assumption that $|r_{Tq}| = 1$ is not valid. Hence, based on the field data it seems that these minima in practice do not reduce the sensitivity of the scintillometer enough to negatively affect the resultant fluxes.

To analyse in more detail why these patterns occur in the field data, for multiple bins we present in Figure 22 the average magnitude and standard error of $\frac{C_{n,mw}^2}{C_T^2}$ together with the average magnitude of the three different terms[19] in Eq. (20).

[19] Note that the slight discrepancy between the sum of the three averaged terms and $\frac{C_{n,mw}^2}{C_T^2}$ is caused by dividing the EC-data into bins and subsequent averaging of each term separately. Then, the sum of the averaged terms is not necessarily equal to the averaged $\frac{C_{n,mw}^2}{C_T^2}$ since the covariance between the terms is not included. This covariance causes the averaged $\frac{C_{n,mw}^2}{C_T^2}$ to be slightly larger than the sum of the averaged terms.

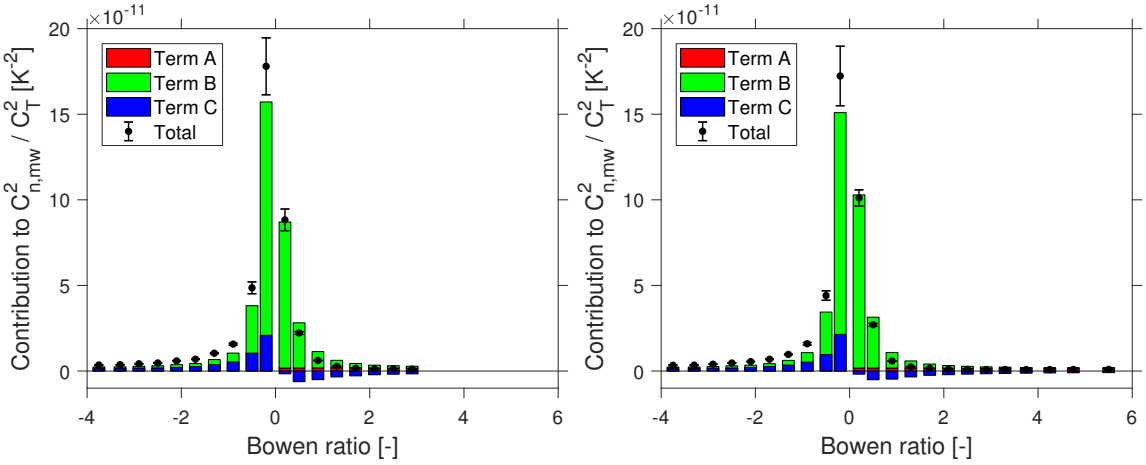

(a) Colza *(b) Rye*

Figure 22: *Magnitude of the three different terms in Eq.*(20) *as function of the Bowen ratio [β]. The black dots with the vertical lines indicate for each bin the average ratio between the structure parameter of the refractive index in the microwave region and the structure parameter of the temperature [$C^2_{n,mw}/C^2_T$], together with the standard error.*

Figure 22 clearly shows that term B (green) becomes dominant for β close to 0, while it decreases rapidly with increasing β. The absolute magnitude of term C also decreases with increasing β, but not as fast as term B and consequently becomes relatively more important at larger $|\beta|$. Furthermore, term C changes sign at β =0 and is negative for positive β. Therefore, as noted before (Section 5.2.2.1) at larger, positive β the decrease in term B is (partly) offset by the decrease in term C (blue), causing a minimum in $\frac{C^2_{n,mw}}{C^2_T}$. Term A (red), on the other hand, does not change with β and appears to be smaller than the other two terms. Hence, term A is not relevant for the behaviour of $\frac{C^2_{n,mw}}{C^2_T}$ as a function of β.

5.2.2.3 Explanation theoretical/observed minima

In the previous two sections we showed based on both theory and field data that $\frac{C^2_{n,mw}}{C^2_T}$ and $\frac{C^2_{n,opt}}{C^2_T}$ have a minimum as a function of the Bowen ratio β. Now, the question remains however why these minima actually occur. We did explain the mathematical behaviour of Eq.20 that resulted in the minima, but did not yet identify the causes behind this behaviour.

To gain more insight into the relevant causes, it is important to realize that $C_{n,\lambda}^2$ is a spatial measure of refractive index fluctuations n' associated with turbulent eddies in the inertial sub-range: according to Eq.(2) $C_{n,\lambda}^2$ is directly connected to the spatial average of the n' occurring at scales within the inertial sub-range, $\overline{(n(x+r)-n(x))^2}$ or simply $\overline{n'^2}$. In this section we will first focus on the individual fluctuations of the refractive index, n', and afterwards discuss in detail the characteristics of $\overline{n'^2}$ that cause the minima.

Individual n' fluctuations

For a certain wavelength λ the refractive index fluctuations n' mainly depend on temperature and humidity fluctuations[20], and can therefore be described with the following formula (Ward et al., 2013, e.g.):

$$n'(\lambda) = A_{t,\lambda}\frac{T'}{\bar{T}} + A_{q,\lambda}\frac{q'}{\bar{q}}, \tag{22}$$

where the primes indicate fluctuations, and $A_{t,\lambda}$, $A_{q,\lambda}$ are dimensionless coefficients that depend on the considered wavelength λ. These coefficients are identical to the ones given in Eq.(6). As said before they are calculated using the expressions given in Ward et al. (2013), which rely on empirical relationships to describe the contribution of dry air and water vapour to the refractive index. A general description of the derivation $A_{t,\lambda}$, $A_{q,\lambda}$ from experimental data for a broad range of wavelengths is given in (Hill et al., 1980), where it is also shown that these coefficients can attain both positive and negative values depending on the wavelength. It is the sign of the coefficients that determines whether temperature and humidity fluctuations lead to a positive or negative n' at a certain wavelength.

Using the expressions given by Ward et al. (2013), one finds that both dimensionless coefficients are negative in the optical range assuming the typical atmospheric conditions given in Table 2. In the microwave range though, $A_{t,mw}$ is negative and $A_{q,mw}$ is positive. This tells us that in the optical range both a positive temperature fluctuation ($T' > 0$) and positive specific humidity fluctuation ($q' > 0$) decrease the refractive index ($n' < 0$). On the contrary, in the microwave range a positive q' increases the refractive index ($n' > 0$), while a positive T' decreases it ($n' < 0$). This difference in signs of the coefficients between the optical and microwave wavelengths will turn out to be crucial for the location of the minima (Table 4).

[20] Pressure fluctuations influence the refractive index as well, but several papers (Hill et al., 1980; Moene et al., 2004; Ward et al., 2013, e.g.) showed that this influence is usually small and can thus be safely neglected.

Besides that, for the location of the minima it is also important to realize that Eq.(22) can become equal to 0 while there are still temperature and humidity fluctuations ($|T'| > 0$ and $|q'| > 0$): the effects of T' and q' on the refractive index can exactly cancel each other if T' and q' have the right ratio. The sign and magnitude of this ratio only depends on the sign and magnitude of the dimensionless coefficients.

Table 3: *The values of the dimensionless coefficients $A_{t,\lambda}$,$A_{q,\lambda}$ for the typical atmospheric conditions given in Table 2.*

	microwave λ	optical λ
$A_{t,\lambda}$	$-4.14 * 10^{-4}$	$-2.70 * 10^{-4}$
$A_{q,\lambda}$	$7.15 * 10^{-5}$	$-6.88 * 10^{-7}$

Characteristics $\overline{n'^2}$ governing presence of minima

Now, in order to understand why and when the theoretical/observed minima occur, we have to focus on $\overline{n'^2}$ since this quantity, and not n', is directly connected to $C^2_{n,\lambda}$. By taking the square and spatial average of Eq.(22), $\overline{n'^2}$ can be written as:

$$\overline{n'^2(\lambda)} = \underbrace{{A_{t,\lambda}}^2 \frac{\overline{T'^2}}{\overline{T^2}}}_{\text{Term I}} + \underbrace{{A_{q,\lambda}}^2 \frac{\overline{q'^2}}{\overline{q^2}}}_{\text{Term II}} + \underbrace{2A_{t,\lambda}A_{q,\lambda}\frac{\overline{T'q'}}{\overline{T}\overline{q}}}_{\text{Term III}} \tag{23}$$

where the bars indicate a spatial average.

As becomes clear from Eq.(23), in total three different terms together determine the magnitude of $\overline{n'^2}$: term I and II reflect the contributions of T' and q' respectively, while term III reflects the effect of the interaction between T' and q'. Terms I and II are always positive, while term III can be both positive and negative. Term III can thus cancel out terms I and II if it is negative.

To illustrate when term III becomes negative, Table 4 shows for optical/microwave wavelengths and positive/negative r_{Tq} the corresponding sings of $A_{t,\lambda}$, $A_{q,\lambda}$, $\overline{T'q'}$, and term III. Since r_{Tq} reflects the correlation between temperature and humidity fluctuations, it has the same sign as $\overline{T'q'}$. Together with the signs of the dimensionless coefficients, this implies that term III is negative for 1) microwave wavelengths and positive r_{Tq}, and 2) optical wavelengths with negative r_{Tq}. Consequently, the minima in $C^2_{n,\lambda}$ only occur with those combinations of λ and r_{Tq} (see Figures 16-20).

Note that the signs of the dimensionless coefficients determine whether the minimum is present at either negative or positive r_{Tq}. Since the signs of the dimensionless coeffcients differ between the optical and microwave wavelengths, the location of the minima thus change as well.

Table 4: *Signs of $A_{t,\lambda}$,$A_{q,\lambda}$,$\overline{T'q'}$ corresponding to positive and negative r_{Tq} for both optical ('opt') and microwave ('mw') wavelengths.*

λ	r_{Tq}	$A_{t,\lambda}$	$A_{q,\lambda}$	$\overline{T'q'}$	Term III Eq.(23)
opt	+	-	-	+	+
opt	-	-	-	-	-
mw	+	-	+	+	-
mw	-	-	+	-	+

The question remains now how these characteristics of Eq.(23) are connected to the Bowen ratio β. To understand this, it is important to realise that $C^2_{n,\lambda}$ has, similarly to β, a dependency on the ratio between $\overline{T'^2}$ and $\overline{q'^2}$: the sum of the three terms in Eq.(23) can reach a minimum when $\overline{T'^2}$ and $\overline{q'^2}$ have the right ratio, comparable to the two terms in Eq.(22). This implies that $\overline{n'^2}$ and thus $C^2_{n,\lambda}$ should show minima as function of β for certain combinations of λ and r_{Tq} (where term III is negative, see Table 4). Hereby, because of the additional third term arising from the squaring and spatial averaging of Eq.(22), $\overline{n'^2}$ can only become 0 when $|r_{Tq}| = 1$. This is consistent with the patterns we observed in Figures 16-20.

5.3 RQ3: Combined Lüdi-Hill method

5.3.1 RQ3: Methods

For this research question, we investigated whether the surface sensible H and latent heat flux LE calculated from the OMS-data improve by implementing a new hybrid method. In this hybrid method cleaned r_{Tq}-values from the Lüdi method (or bichromatic method) are used as input for the Hill method (or two-wavelength method).

Here, the main issue is how to clean r_{Tq} such that the erratic behaviour from the Lüdi method is removed, but at the same time the real, physical changes are retained. By experimenting with different settings and analysing resulting time-series, we eventually decided to implement the following cleaning steps for r_{Tq} in the hybrid method:

1. Remove unrealistic values where $|r_{Tq}| \geq 1$. $|r_{Tq}|$-values between 1 and 4 were set to 0.8 and -0.6 for positive and negative r_{Tq} respectively (consistent with Figure 21), while values above 4 were completely removed.

2. Remove erratic sign-changes, where a r_{Tq}-value corresponding to one interval is defined as an erratic sign change when the surrounding two intervals have both an opposite sign. Then, the r_{Tq}-value of that specific interval is replaced by the r_{Tq}-value of the preceding interval. So, if for instance one negative r_{Tq}-value is preceded and followed by a positive r_{Tq}-value, the negative r_{Tq}-value is classified as a erratic sign change and replaced by the positive r_{Tq}-value preceding it.

3. Smooth the r_{Tq}-values by applying a moving average with a window size equal to 5 intervals.

After these cleaning steps, the resulting r_{Tq}-values are used to prescribe r_{Tq} in the Hill-method. Relying on auxiliary measurements from the meteorological tower in Lindenberg (Section 4.1), we calculated C_T^2, C_q^2-values that were consistent with the derived r_{Tq}-values. To determine subsequently the surface fluxes H and LE in the third processing step (Section 2.3.3, we additionally assumed typical values for the roughness length z_0 ($0.2m$), the latent heat of vaporization L_v ($2.46 * 10^6 J/kg$), and the air density ρ ($1.2kg/m^3$).

Hereby, it is important to note that the sign of r_{Tq} determines whether the unstable or stable MOST-relationships are used (see Section 2.3.3). For this reason we included in the hybrid method a quality flag that indicates how reliable the sign of r_{Tq} is, based on the r_{Tq}-values obtained after the three cleaning steps described above. The score of the flag we implemented varies between 0 (very unreliabe) to 1 (very reliable), and is calculated using the following simple formula:

$$flag = |r_{Tq}| * (1 - \overline{std(r_{Tq})}), \tag{24}$$

where $\overline{std(r_{Tq})}$ indicates a moving average of the standard deviation over five 10-minute intervals[21]. The rationale behind Eq.(24) is that the sign of r_{Tq} is very uncertain when $|r_{Tq}|$ and/or the standard deviation are (is) high, which would result in a score close to 0. By analysing the scores of the flag for different $|r_{Tq}|$-values, we chose 0.3 as a threshold to decide whether the sign of $|r_{Tq}|$ is reliable or not.

[21] Note that $|r_{Tq}|$ and the moving average of the standard deviation cannot be higher than 1 because of the cleaning, which implies that the score of the flag can only vary between 0 and 1.

For all intervals where the score is lower than 0.3, the sign of $|r_{Tq}|$ is classified as unreliable. In that way, this flag can quickly identify in which intervals large errors could be present in the calculated surface fluxes.

Hereby, it should be noted that we applied some of the spectral filters developed in the first research question (see Section 5.1.1):

1. A strict HPF for the MWS-signal (where 90% of the theoretical variance is retained for a typical minimum cross-wind speed of $0.5m/s$).
2. A loose HPF for the LAS-signal (where 99% of the theoretical variance is retained for a typical minimum cross-wind speed of $0.5m/s$).
3. The spike filter as described in Section 5.1.1.2.

5.3.2 RQ3: Results

In this section, we will illustrate the differences between the Hill, Lüdi, and newly developed hybrid method by showing r_{Tq}, H, and LE for two different time periods as an example (Figure 23 and 24).

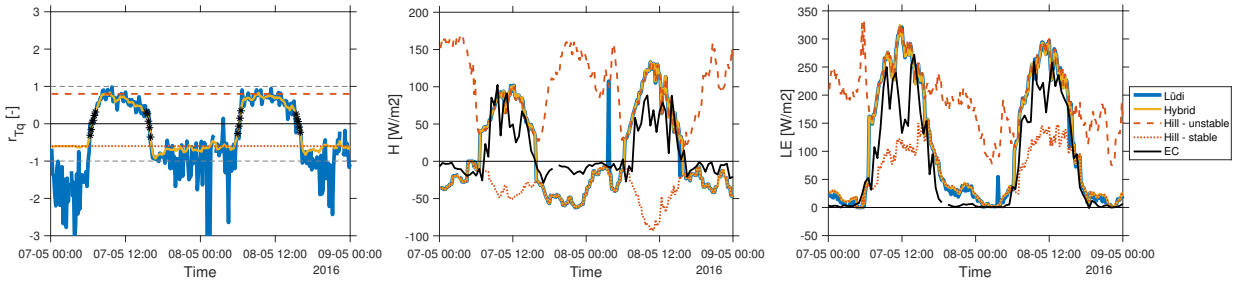

(a) *(b)* *(c)*

Figure 23: *Time-series of r_{Tq} (a), H (b), LE(c) for the period from 7 up to 9 May 2016, where the colours indicate the different methods. Note that for the Hill-method both the unstable and stable solution are given, where r_{Tq} is chosen to be equal to 0.8 and -0.6 respectively. The black starts in panel (a) indicate intervals where the quality flag described in Section 5.3.1 is below 0.3 and thus the sign of r_{Tq} is classified as unreliable.*

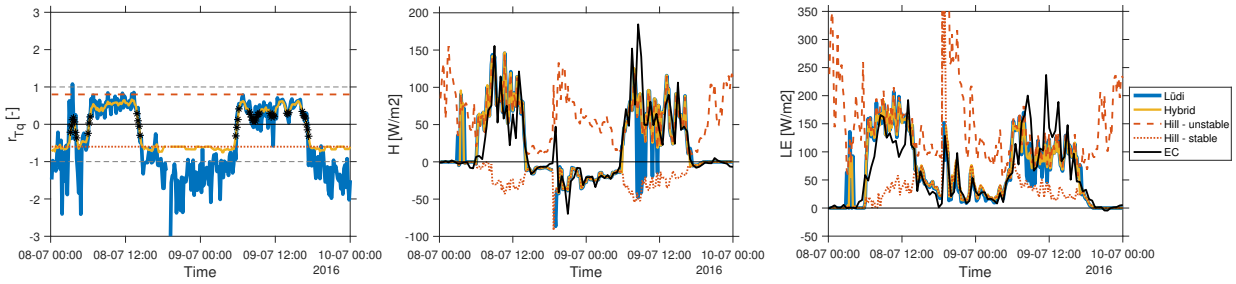

(a) *(b)* *(c)*

Figure 24: *Time-series of r_{Tq} (a), H (b), LE(c) for the period from 8 up to 10 July 2016, where the colours indicate the different methods. Note that for the Hill-method both the unstable and stable solution are given, where r_{Tq} is chosen to be equal to 0.8 and -0.6 respectively. The black starts in panel (a) indicate intervals where the quality flag described in Section 5.3.1 is below 0.3 and thus the sign of r_{Tq} is classified as unreliable.*

Focusing first on the time-series of r_{Tq} (Figure 23a and 24a), there are clear differences between the three methods. The Hill-method has fixed values for r_{Tq} (in this case 0.8 and -0.6), and has both a positive (unstable) and negative (stable) solution. In contrast, the Lüdi and hybrid method only have one solution. Comparing the Lüdi and hybrid method, the hybrid method clearly provides more realistic r_{Tq}-values because: 1) the hybrid method shows much less erratic behaviour, and 2) the hybrid method does not give unrealistic values (where $|r_{Tq}| \geq 1$).

Looking in more detail to the impact of these differences in r_{Tq} for H (Figure 23b and 24b) and LE (Figure 23c and 24c), we see though that the exact calculated value of r_{Tq} barely matters. In case of H, the results of the different methods are even identical.

However, large differences in the LE and especially H do arise when the r_{Tq} changes sign between the methods. As explained in Section 5.3.1, the sign of r_{Tq} has a large impact on the surface fluxes because it is used to choose between the stable- and unstable MOST relationships. The hybrid and Lüdi method seem to do in general a good job: the calculated H and LE agree in most cases reasonably well with the EC-measurements, indicating that both methods usually choose the right sign. This is a clear advantage over the Hill method.

Especially the Lüdi method though is sometimes affected by sign-changes in r_{Tq}, which seem to be caused by erratic behaviour rather than real changes in stability.

Considering for instance the day of 9 July, the Lüdi method shows as a consequence of this erratic behaviour large errors in H and LE during some intervals. The hybrid method resolves these erratic sign-changes in the Lüdi method quite well, providing more realistic H and LE. However, we should also note that there are some intervals (e.g. during the night of 8 July) where the hybrid method does not resolve the erratic sign-changes present in the Lüdi method.

This is the reason why we implemented a quality flag in the hybrid method that quickly identifies the intervals where the sign of r_{Tq} is not reliable (Figure 23a and 24a), enabling possible future users to assess whether the provided sign is correct only in cases where the hybrid method is likely to be unreliable. In that way the intervals where the hybrid method does not remove the erratic sign-changes, can be quickly identified and changed accordingly. Because of this the hybrid method has the potential to improve the calculated surface fluxes H and LE, especially when the Lüdi method shows strong erratic sign changes in r_{Tq}.

Finally, we would like to note that the implemented spectral filters (Section 5.3.1) already partly removed the erratic behaviour of the Lüdi-method. On the other hand, using a 30-minute interval instead of a shorter 1- or 10-minute interval will reduce the observed erratic behaviour. However, in practise the shorter intervals are used often. For this reason we only showed the results corresponding to 10-minute intervals (see Section 4.2).

6 Conclusions

In this research the overall aim was to improve the accuracy of the surface fluxes determined from combined Optical-Microwave Scintillometers (OMS) measurements: we focused on three different issues related to the required processing of the raw measurements, which can negatively affect the quality of the calculated fluxes. Hereby, we relied on OMS and EC-data from the meteorological observatory in Lindenberg, Eastern Germany (operated by the Deutsche WetterDienst, DWD) and surroundings. This area is characterised by a heterogeneous landscape, consisting of patches with different types of land-use. In the past decade multiple large field campaigns have been conducted here, which are commonly referred to under the acronym LITFASS (Beyrich et al., 2006, 2012, e.g.).

We will present below for each of the three investigated issues the posed research question, together with a summary of our main findings:

1. *What is the most optimal fixed band-pass filter (BPF) to filter out unwanted contributions from the raw scintillation signal, taking into account the measured cross-wind regime, the characteristics of the measurement set-up, and a newly developed spike filter?*

In order to take into account the measured cross-wind regime and the characteristics of the measurement set-up, we developed a new systematic framework to choose an appropriate BPF based on the real part of the theoretical spectrum from Clifford (1971). This framework is set-up such that it can also be easily applied to other datasets.

Hereby, it was striking that a high-pass filter (HPF) had a much larger impact on the calculated variances than a low-pass filter (LPF). As a consequence the HPF appeared to be most relevant for the performance of the method, clearly causing an improvement when comparing the OMS data to EC-measurements. For the OMS in Lindenberg a loose HPF (where 90% of the variance from the spectrum of Clifford (1971) is retained for a typical minimum cross-wind speed of 0.5m/s) seemed to be most suitable for the LAS, while a more strict HPF seemed to be appropriate for the MWS (where 99% of the variance from the theoretical spectrum of Clifford (1971) is retained for typical minimum cross-wind speed of 0.5m/s). However, we were not able to detect a clear improvement when a LPF was included.

2. *How does $C_{n,\lambda}^2$ depend on the Bowen ratio and the correlation coefficient between temperature and humidity for both optical and microwave wavelengths, and what are the consequences of these relations for the practical usability of the optical-microwave scintillometers?*

This research question followed from investigating in detail the claim made in literature that $C_{n,mw}^2$ reached a minimum around $\beta \approx 2-3$, which even becomes equal to 0 when $|r_{Tq}| = 1$ (Leijnse et al., 2007; Ward et al., 2013). We derived a new analytical expression that describes $C_{n,\lambda}^2$ (scaled with C_T^2) directly as a function of β for given r_{Tq}. Using this new expression we were not only able to confirm the minimum reported in literature, but also found a second minimum of $C_{n,opt}^2$ for negative β close to 0.

Since these two theoretical minima could reduce the sensitivity of the OMS, we investigated whether they also occurred in experimental EC-data from two stations a few meters above a colza and rye field. The theoretical minima indeed appeared to be present, but were not very pronounced since in reality $|r_{Tq}| \neq 1$. Hence, in practice these two minima likely do not hamper the sensitivity of the OMS-instrument.

3. *Can the derived surface fluxes (H,LE) be improved by using cleaned r_{Tq}-values found with the bichromatic method described by Lüdi et al. (2005), as input for the two-wavelength method described by Hill (1997)?*

To tackle this research question, we developed a new hybrid method that removes partly the erratic behaviour of the r_{Tq}-values from the Lüdi method (or bichromatic method). Subsequently, the new r_{Tq}-values are applied in the more robust Hill method (or two-wavelength method) to derive consistent surface fluxes.

The hybrid method appeared to be mainly beneficial when the Lüdi method showed erratic sign-changes, since the sign of r_{Tq} determines whether the unstable or stable MOST-relationships need to be used. This has a large influence on the calculated fluxes, and consequently these erratic sign changes cause large errors in the Lüdi method. The hybrid method resolves most of these erratic sign changes, but not all of them. For this reason we included a quality flag in the hybrid method that indicates when the sign of r_{Tq} is not reliable. This allows potential future users to identify quickly the intervals where the hybrid possibly gives the wrong sign, and replace the surface fluxes in those intervals with the ones corresponding to the other solution if needed.

7 Recommendations

Based on our research, we have multiple concrete recommendations to improve the quality of the surface fluxes determined from OMS-data. Additionally, we have one recommendation for future research. Below, we will list each of them:

1. In the software belonging to the MWS used in this experiment (see Section 4.1) currently only a user-defined HPF is included (RPG, 2018). We recommend to incorporate in the software the framework developed in this study, such that the user only has to specify the theoretical retained variance fraction and typical minimum/maximum cross-wind speeds for a given scintillometer set-up. In that way the filters are defined in a more user-friendly way, especially when the user does not have a lot of experience with scintillometers and thus does not know what a suitable HPF is. Furthermore, we recommend to include a LPF between 100-200 Hz: although we did not find a clear improvement in our analysis when we implemented a LPF, in some cases it does seem to remove unwanted contributions to the signal (especially when the scintillometer considered is very sensitive to electronic noise).

2. For the LAS used in this research (see Section 4.1) currently the HPF is often set to 0.1Hz, while the LPF is set to 400Hz (Moene et al., 2005)). The value for the HPF seems to be reasonable in most cases, but we do recommend to set at least the LPF much lower to ensure that more unwanted contributions are removed (between 100-200Hz). Furthermore, similar as for the MWS we recommend to implement the framework developed in this study.

3. For both the LAS and MWS we recommend to incorporate also a spike filter similar to the one deployed in this study, especially when it is crucial to have very accurate fluxes. Mainly during neutral/stable conditions with low fluxes, the influence of the spikes can sometimes be substantial. Hereby, the computation time can be reduced by implementing a LPF.

4. In case the bichromatic method described by Lüdi et al. (2005) is affected by strong erratic sign changes in r_{Tq}, we recommend to use instead the hybrid method developed in this study. The hybrid method resolves in most cases quite well erratic sign changes in r_{Tq}, giving more realistic values for H and LE. Furthermore, it provides a quality flag that identifies the intervals where the sign of r_{Tq} is unreliable and thus the calculated surface fluxes may show large errors.

Hereby we recommend to store the fluxes corresponding to both the unstable and stable MOST-relationships, enabling users to replace the fluxes with the ones corresponding to the other solution when appropriate.

5. For future research we recommend to repeat the comparison with EC-data done in this research using a simpler dataset, where the OMS is located close to the surface and in a homogeneous environment. In that case, an EC-station located close to the OMS can properly serve as a reference without the complications that arose in this study (see Section 5.1.1.3). There are currently plans to install such a set-up at Cabauw in the Netherlands, where the surroundings dominantly exist of flat grassland.

Appendices

A: Derivation of Eq.(20) and alternative formulation based on available energy Q

In this derivation we will show step-by-step how Eq.(6) can be rewritten in terms of β and r_{Tq}, which eventually leads to the expression given in Eq.(20). Furthermore, to complement the results given in Leijnse et al. (2007) and Ward et al. (2013) we will present an alternative formulation of Eq.(20) that additionally uses the available energy Q. As explained in Section 5.2.2.1, we did not use this alternative formulation because the dependency on Q makes a comparison of the analytical solution with the experimental EC-data shown in Section 5.2.2.2 more difficult.

For this derivation, we will use 1) the definition of r_{Tq} given in Eq.(7), 2) an equation that connects β to C_T^2 and C_q^2, and 3) an equation that connects C_T^2 to Q and β. The resulting system of equations can be written as:

$$\begin{cases} C_{n,\lambda^2} = A_{t,\lambda}^2 \dfrac{C_T^2}{\bar{T}^2} + A_{q,\lambda}^2 \dfrac{C_q^2}{\bar{q}^2} + 2A_{t,\lambda}A_{q,\lambda} \dfrac{C_{Tq}}{\bar{T}^2\bar{q}^2}, & (6) \\ r_{Tq} = \dfrac{C_{Tq}}{\sqrt{C_T^2 C_q^2}}, & (7) \\ \beta = sgn(r_{Tq}) \dfrac{c_p}{L_v} \sqrt{\dfrac{C_T^2}{C_q^2}}, & (A.1) \\ C_T^2 = \dfrac{Q^2 f_{C_T^2}}{\rho^2 c_p^2 u_*^2 z^{2/3} (1 + \frac{1}{\beta^2})}. & (A.2) \end{cases}$$

In this appendix, we will first give a derivation of Eq.(A.1) and Eq.(A.2) in Sections A.1 and A.2 respectively. Subsequently, in Section A.3 we will show how this system of equations can be solved to derive Eq.(20) together with the alternative formulation based on Q.

A.1: Derivation of Eq.(A.1)

In this section we will show how the Bowen ratio β can be expressed in terms of the structure parameters C_T^2 and C_q^2. As a starting point, we use the following definition of the Bowen ratio:

$$\beta \equiv \frac{H}{LE}, \text{where } H = \rho c_p \overline{w'T'} \text{ and } LE = L_v \rho \frac{\overline{w'q'}}{1-\overline{q}}. \tag{A.3}$$

Here, ρ indicates the density of air $[\frac{kg}{m^3}]$, c_p the heat capacity of air at constant pressure ($= 1005\ [\frac{J}{kg*K}]$),T the temperature $[K]$, L_v the latent heat of vaporization ($= 2.46 * 10^6\ [\frac{J}{kg}]$), and q the specific humidity $[\frac{kg}{kg}]$. The factor $\frac{1}{1-\overline{q}}$ arises because the water vapour flux itself affects the air density [22] (Webb et al., 1980). Note that we assumed the fluctuations in absolute temperature T are directly proportional to H, rather than the fluctuations in potential temperature. For an EC-system close to the surface, this assumption is reasonable since the horizontal and vertical pressure differences near the system are small.

The structure parameters C_T^2 and C_q^2 are connected to H and LE via the dimensionless MOST-groups $f_{C_T^2}$ and $f_{C_q^2}$:

$$f_{C_T^2} = \frac{C_T^2 z^{2/3}}{T_*^2}, \tag{A.4}$$

$$f_{C_q^2} = \frac{C_q^2 z^{2/3}}{q_*^2}. \tag{A.5}$$

Here, $T_* = -\frac{\overline{w'T'}}{u_*}$ and $q_* = \frac{\overline{w'q'}}{u_*}$ with u_* being the friction velocity $[\frac{m}{s}]$. Relying on these definitions for T_* and q_*, we can write H and LE in terms of C_T^2 and C_q^2 via Eq.(A.4) and (A.5):

$$H^2 = \rho^2 c_p^2 u_*^2 z^{2/3} \frac{C_T^2}{f_{C_T^2}} \tag{A.6}$$

$$LE^2 = \frac{\rho^2 L_v^2 u_*^2 z^{2/3}}{(1-\overline{q})^2} \frac{C_q^2}{f_{C_q^2}} \tag{A.7}$$

[22] Webb et al. (1980) explain that there is a small mean vertical upward velocity caused by density effects of the water vapour flux: rising moist air parcels are less dense than the descending drier air parcels, which induces a mean upward flow assuming there is no net air mass exchange in the vertical. This mean upward flow, in turn, also transports water vapour and thus contributes to the latent heat flux. In EC-measurements however, this is not taken into account: only the velocity fluctuations relative to the mean vertical velocity are considered. Hence, EC-measurements need to be corrected for these density effects.

Next we will take the square root of (A.6) and (A.7), and subsequently substitute them in (A.3). However, by taking the square root possible negative values of H and LE are eliminated. To retain the sign of the Bowen ratio, we will include the sign of r_{Tq} (for the definition of r_{Tq} see Eq.(7)). r_{Tq} indicates whether H and LE act in the same direction (when $r_{Tq} > 0$) or not (when $r_{Tq} < 0$).

Besides that, we will assume that the dimensionless MOST-groups $f_{C_T^2}$ and $f_{C_q^2}$ are equal for both stable and unstable conditions. This is true when MOST is strictly valid (i.e under homogeneous and stationary conditions), and as a consequence $|r_{Tq}| = 1$ (Hill, 1989). In practice, the MOST-groups can differ because of a dissimilar transport efficiency, non-local effects (such as advection, entrainment), and/or differences in the spatial distribution of the heat and water vapour sources (which occurs for instance in a field with patchy vegetation or in a forest) (De Bruin et al., 1999; Kooijmans and Hartogensis, 2016).

Assuming also that $(1 - \overline{q}) \approx 1$, the Bowen ratio can be expressed as follows (Andreas, 1990; Ward et al., 2015a, e.g.):

$$\beta = sgn(r_{Tq}) \frac{c_p}{L_v} \sqrt{\frac{C_T^2}{C_q^2}} \tag{A.1}$$

A.2: Derivation of Eq.(A.2)

In this section we will show the derivation of Eq.(A.2), which is only needed for the alternative formulation of Eq.(20) (see Section A.3). The available energy Q is simply the sum of the sensible and latent heat flux. Using the definition of the Bowen ratio (Eq.(A.3)) and Eq.(A.6), Q^2 can be expressed as:

$$Q^2 = H^2 + LE^2 = H^2 + \frac{H^2}{\beta^2} = \rho^2 c_p^2 u_*^2 z^{2/3} \frac{C_T^2}{f_{C_T^2}} (1 + \frac{1}{\beta^2}). \tag{A.8}$$

Rearranging gives:

$$C_T^2 = \frac{Q^2 f_{C_T^2}}{\rho^2 c_p^2 u_*^2 z^{2/3} (1 + \frac{1}{\beta^2})}. \tag{A.2}$$

A.3: Solving system of equations (Eq.(6),(7),(A.1),(A.2))

In this section, using the system of equations given at the beginning of this appendix we will first derive Eq.(20), and subsequently show an alternative formulation based on Q. As a first step, we substitute Eq.(7) into Eq.(6) and divide by $\sqrt{C_T^2 C_q^2}$. This gives:

$$\frac{C_{n,\lambda}^2}{\sqrt{C_T^2 C_q^2}} = \frac{A_{t,\lambda}^2}{\overline{T}^2}\sqrt{\frac{C_T^2}{C_q^2}} + \frac{A_{q,\lambda}^2}{\overline{q}^2}\sqrt{\frac{C_q^2}{C_T^2}} + 2|r_{Tq}|\frac{A_{t,\lambda}A_{q,\lambda}}{\overline{T}\,\overline{q}} \tag{A.9}$$

Next, we substitute Eq.(A.1) in Eq.(A.9) to get eventually Eq.(20) that describes $C_{n,\lambda}^2$ as a function of β (realizing that $sgn(r_{Tq})r_{Tq} = |r_{Tq}|$):

$$\frac{C_{n,\lambda}^2}{C_T^2} = \frac{A_{t,\lambda}^2}{\overline{T}^2} + \frac{A_{q,\lambda}^2}{\overline{q}^2}\frac{c_p^2}{L_v^2\beta^2} + 2|r_{Tq}|\frac{A_{t,\lambda}A_{q,\lambda}}{\overline{T}\,\overline{q}}\frac{c_p}{L_v\beta} \tag{20}$$

When $|r_{Tq}| = 1$, this can be simplified to:

$$\frac{C_{n,\lambda}^2}{C_T^2} = (\frac{A_{t,\lambda}}{\overline{T}} + \frac{A_{q,\lambda}}{\overline{q}}\frac{c_p}{L_v\beta})^2, \tag{A.10}$$

which shows that β has a non-trivial solution ($\beta \neq 0$) for $\frac{C_{n,\lambda}^2}{C_T^2} = 0$. This is consistent with the observation that $\frac{C_{n,\lambda}^2}{C_T^2}$ is equal to 0 for certain β-values when $|r_{Tq}| = 1$ (see Section 5.2.2.1).

Finally, Eq.(20) can be alternatively formulated based on Q by substituting Eq.(A.2):

$$C_{n,\lambda}^2 = (\frac{A_{t,\lambda}^2}{\overline{T}^2} + \frac{A_{q,\lambda}^2}{\overline{q}^2}\frac{c_p^2}{L_v^2\beta^2} + 2|r_{Tq}|\frac{A_{t,\lambda}A_{q,\lambda}}{\overline{T}\,\overline{q}}\frac{c_p}{L_v\beta})\frac{Q^2 f_{C_T^2}}{\rho^2 c_p^2 u_*^2 z^{2/3}(1+\frac{1}{\beta^2})}, \tag{A.11}$$

where it should be noted that $f_{C_T^2}$ depends on the stability parameter $\frac{z}{L_o}$ (Eq.(14)-(16)). This implies that Eq.(A.11) can only be solved implicitly.

Leijnse et al. (2007) and Ward et al. (2013) prescribed Q which allowed them to calculate $C_{n,\lambda}^2$ directly rather than the ratio $\frac{C_{n,\lambda}^2}{C_T^2}$. However, this has the important disadvantage that the results are then only valid for the prescribed Q. The analytical solution can be more easily compared to experimental EC-data if there is no dependency on Q: the EC-data is continuously affected by changes in available energy. Therefore, we have decided to use instead the expression given in Eq.(20), which is universal for all available energies Q.

References

EL Andreas. Three-wavelength method of measuring path-averaged turbulent heat fluxes. *Journal of Atmospheric and Oceanic Technology*, 7(6): 801–814, 1990.

WGM Bastiaanssen, M Menenti, RA Feddes, and AAM Holtslag. A remote sensing surface energy balance algorithm for land (SEBAL). 1. formulation. *Journal of hydrology*, 212:198–212, 1998.

F Beyrich, JP Leps, M Mauder, J Bange, T Foken, S Huneke, H Lohse, A Lüdi, WML Meijninger, D Mironov, et al. Area-averaged surface fluxes over the LITFASS region based on eddy-covariance measurements. *Boundary-layer meteorology*, 121(1):33–65, 2006.

F Beyrich, J Bange, OK Hartogensis, S Raasch, M Braam, D van Dinther, D Gräf, B van Kesteren, AC van den Kroonenberg, B Maronga, et al. Towards a validation of scintillometer measurements: the LITFASS-2009 experiment. *Boundary-layer meteorology*, 144(1):83–112, 2012.

M Braam. *Aspects of atmospheric turbulence related to scintillometry*. PhD thesis, Wageningen University and Research, 2014.

SF Clifford. Temporal-frequency spectra for a spherical wave propagating through atmospheric turbulence. *JOSA*, 61(10):1285–1292, 1971.

HAR De Bruin, BJJM Van Den Hurk, and LJM Kroon. On the temperature-humidity correlation and similarity. *Boundary-Layer Meteorology*, 93(3): 453–468, 1999.

AE Green, SR Green, MS Astill, and HW Caspari. Estimation latent heat flux form a vineyard using scintillometry. *Terrestrial, Atmospheric and Oceanic Sciences*, 11(2):525–542, 2000.

OK Hartogensis. *Exploring scintillometry in the stable atmospheric surface layer*. PhD thesis, Wageningen University and Research, 2006.

RJ Hill. Implications of Monin–Obukhov similarity theory for scalar quantities. *Journal of the Atmospheric Sciences*, 46(14):2236–2244, 1989.

RJ Hill. Algorithms for obtaining atmospheric surface-layer fluxes from scintillation measurements. *Journal of Atmospheric and Oceanic Technology*, 14(3):456–467, 1997.

RJ Hill, SF Clifford, and RS Lawrence. Refractive-index and absorption fluctuations in the infrared caused by temperature, humidity, and pressure fluctuations. *JOSA*, 70(10):1192–1205, 1980.

JCB Hoedjes, A Chehbouni, J Ezzahar, R Escadafal, and HAR De Bruin. Comparison of large aperture scintillometer and eddy covariance measurements: Can thermal infrared data be used to capture footprint-induced differences? *Journal of Hydrometeorology*, 8(2):144–159, 2007.

W Kohsiek, WML Meijninger, HAR DeBruin, and F Beyrich. Saturation of the large aperture scintillometer. *Boundary-layer meteorology*, 121(1): 111–126, 2006.

AN Kolmogorov. The local structure of turbulence in incompressible viscous fluid for very large reynolds numbers. *Dokl. Akad. Nauk SSSR*, 30(4): 299–303, 1941.

LMJ Kooijmans and OK Hartogensis. Surface-layer similarity functions for dissipation rate and structure parameters of temperature and humidity based on eleven field experiments. *Boundary-Layer Meteorology*, 160(3): 501–527, 2016.

RS Lawrence, GR Ochs, and SF Clifford. Use of scintillations to measure average wind across a light beam. *Applied Optics*, 11(2):239–243, 1972.

MY Leclerc and GW Thurtell. Footprint prediction of scalar fluxes using a Markovian analysis. *Boundary-Layer Meteorology*, 52(3):247–258, 1990.

H Leijnse, R Uijlenhoet, and JNM Stricker. Hydrometeorological application of a microwave link: 2. precipitation. *Water resources research*, 43(4), 2007.

A Lüdi, F Beyrich, and C Mätzler. Determination of the turbulent temperature–humidity correlation from scintillometric measurements. *Boundary-layer meteorology*, 117(3):525–550, 2005.

V Masson. Urban surface modeling and the meso-scale impact of cities. *Theoretical and applied climatology*, 84(1-3):35–45, 2006.

WML Meijninger, AE Green, OK Hartogensis, W Kohsiek, JCB Hoedjes, RM Zuurbier, and HAR De Bruin. Determination of area-averaged water vapour fluxes with large aperture and radio wave scintillometers over a heterogeneous surface–Flevoland field experiment. *Boundary-Layer Meteorology*, 105(1):63–83, 2002.

WML Meijninger, F Beyrich, A Lüdi, W Kohsiek, and HAR De Bruin. Scintillometer-based turbulent fluxes of sensible and latent heat over a heterogeneous land surface–a contribution to LITFASS-2003. *Boundary-Layer Meteorology*, 121(1):89–110, 2006.

X Mo, S Liu, Z Lin, Y Xu, Y Xiang, and TR McVicar. Prediction of crop yield, water consumption and water use efficiency with a SVAT-crop

growth model using remotely sensed data on the North China Plain. *Ecological Modelling*, 183(2):301–322, 2005.

AF Moene, WML Meijninger, OK Hartogensis, W Kohsiek, and HAR De Bruin. A review of the relationships describing the signal of a large aperture scintillometer. *Internal report 2004/2, Meteorology and Air Quality Group, Wageningen University and Research, Wageningen, the Netherlands*, 2004.

AF Moene, W Meijninger, OK Hartogensis, B Heusinkveld, and HAR De Bruin. The effect of finite accuracy in the manufacturing of large aperture scintillometers. *Internal report 2005-1, Meteorology and Air Quality Group, Wageningen University and Research, Wageningen, the Netherlands*, 2005.

AS Monin and AM Obukhov. Basic laws of turbulent mixing in the atmosphere near the ground. *Tr. Akad. Nauk SSSR Geophiz. Inst*, 24(151): 163–187, 1954.

GR Ochs, SF Clifford, and T Wang. Laser wind sensing: the effects of saturation of scintillation. *Applied optics*, 15(2):403–408, 1976.

RPG. *RPG-MWSC-160 Microwave Scintillometer Operation and Software Guide Version 1.21*, 2018.

PA Solignac, A Brut, JL Selves, JP Béteille, and JP Gastellu-Etchegorry. Attenuating the absorption contribution on C_n^2 estimates with a large-aperture scintillometer. *Boundary-layer meteorology*, 143(2):261–283, 2012.

RB Stull. *An introduction to boundary layer meteorology*. Springer Science & Business Media, 1988.

VI Tatarskii. Wave propagation in turbulent medium. *Wave Propagation in Turbulent Medium, by Valerian Ilich Tatarskii. Translated by RA Silverman. 285pp. Published by McGraw-Hill, 1961.*, 1961.

D van Dinther, OK Hartogensis, and AF Moene. Crosswinds from a single-aperture scintillometer using spectral techniques. *Journal of atmospheric and oceanic technology*, 30(1):3–21, 2013.

B van Kesteren, F Beyrich, OK Hartogensis, and M Braam. Long-term evaluation of the Scintec boundary-layer scintillometer and the Wageningen large-aperture scintillometer: implications for scintillometer users. *Boundary-layer meteorology*, 156(2):303–323, 2015.

T Wang, GR Ochs, and SF Clifford. A saturation-resistant optical scintillometer to measure C_n^2. *JOSA*, 68(3):334–338, 1978.

HC Ward, JG Evans, OK Hartogensis, AF Moene, HAR De Bruin, and CSB Grimmond. A critical revision of the estimation of the latent heat flux from two-wavelength scintillometry. *Quarterly Journal of the Royal Meteorological Society*, 139(676):1912–1922, 2013.

HC Ward, JG Evans, CSB Grimmond, and J Bradford. Infrared and millimetre-wave scintillometry in the suburban environment–Part 1: Structure parameters. *Atmospheric Measurement Techniques*, 8(3):1385–1405, 2015a.

HC Ward, JG Evans, and CSB Grimmond. Infrared and millimetre-wave scintillometry in the suburban environment–Part 2: Large-area sensible and latent heat fluxes. *Atmospheric Measurement Techniques*, 8(3):1407–1424, 2015b.

EK Webb, GI Pearman, and R Leuning. Correction of flux measurements for density effects due to heat and water vapour transfer. *Quarterly Journal of the Royal Meteorological Society*, 106(447):85–100, 1980.

C-Y Xu and VP Singh. Review on regional water resources assessment models under stationary and changing climate. *Water resources management*, 18(6):591–612, 2004.